4 Surfaces and Interfaces of Sputter-Deposited ZnO Films

A. Klein and F. Säuberlich

In this chapter chemical and electronic surface and interface properties of magnetron sputtered ZnO films as determined from photoelectron spectroscopy are described. We particularly focus on interfaces that are important for $Cu(In,Ga)Se_2$ thin film solar cells. The use of in situ sample preparation utilizing integrated vacuum systems allows for systematic studies widely ruling out the influence of adsorbates on the electronic structure. No evidence for band bending at the surface is observed indicating the absence of surface states in the band gap. The ionization potential varies with deposition conditions, which can be attributed to changes in crystallographic orientation of the films resulting in different surface terminations. A variation of the Zn 2p and O 1s core level binding energies with respect to the valence band maximum is attributed to local disorder in films deposited from ceramic ZnO targets at room temperature without addition of oxygen to the sputter gas.

In the interface studies, no effects attributable to *sputter damage* could be identified. The surface and interface chemistry of sputtered ZnO films is rather governed by the ability of the surfaces to dissociate the oxygen molecules condensing from the gas phase. Poor oxygen dissociation on ZnO and CdS leads to the presence of peroxides on the ZnO surfaces and to a nonreactive interface between CdS and ZnO. Noticeable interface reactions are observed between $Cu(In,Ga)Se_2$ or In_2S_3 and ZnO, where no peroxide species is observed during initial ZnO growth. The variation of the core-level binding energies with respect to the valence band maximum leads to an apparent variation of the band alignment at the CdS/ZnO[1] interface with deposition conditions. The band alignment is strongly influenced by Fermi level pinning, which is particularly pronounced at In_2S_3/ZnO interfaces. The observed variation of band alignment at these interfaces can be related to observed efficiencies of $Cu(In,Ga)Se_2$ solar cells using In_2S_3 buffer layers. An amorphous nucleation layer of 2–3 nm thickness is observed for sputter deposition of ZnO films on all investigated substrates. The amorphous layer leads to a modification of the band alignment at the CdS/ZnO interface compared with the reverse deposition sequence (ZnO/CdS).

[1] We generally use the notation substrate/overlayer throughout this chapter.

4.1 Introduction

4.1.1 Semiconductor Interfaces

Transparent conducting oxides are widely used as electrodes in thin film optoelectronic devices as solar cells and light emitting diodes because of their transparency for visible light and their high electrical conductivity. Highest optical transparency and electrical conductivity are thus key aspects for such applications. Most work on TCO electrodes is, therefore, dedicated to find deposition parameters, which improve these material parameters. In addition, contact properties are essential for the application of TCOs as electrodes.

To elucidate the contact properties, the energy band diagrams of the devices have to be considered. Figure 4.1 shows energy band diagrams of two basic semiconductor contacts, a semiconductor/metal contact and a semiconductor p/n- heterocontact. Basic interface parameters are the Schottky barrier height $\Phi_B = E_F - E_{VB}$ for p-type and $\Phi_B = E_{CB} - E_F$ for n-type semiconductors, and the valence and conduction band offsets ΔE_{VB} and ΔE_{CB}. The potential distribution across an interface is determined by the barrier heights and by the doping profile. As doping of semiconductors is typically well controlled [1], the energy band diagrams of semiconductor contacts, which determines the function of the device, can usually be well predicted and modified if the barrier heights are known.

Extensive research has been devoted in the past to understand the mechanisms governing barrier formation at semiconductor interfaces to enable prediction and possible modification of barrier heights [2–8]. An essential feature of semiconductor interfaces is *Fermi level pinning*, which leads to barrier heights at semiconductor/metal contacts being almost independent on the metal. Fermi level pinning is especially pronounced for semiconductors with covalent bonding such as Si, Ge, and GaAs. It occurs even for defect-free

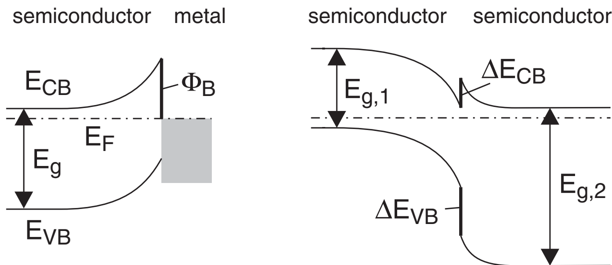

Fig. 4.1. Example energy band diagrams for a semiconductor/metal contact and and a semiconductor p/n-heterocontact. The Schottky barrier height for electrons $\Phi_{B,n}$ is given by the energy difference of the conduction band minimum E_{CB} and the Fermi energy E_F. The valence and conduction band offsets ΔE_{VB} and ΔE_{CB} are given by the discontinuities in the valence band maximum E_{VB} and the conduction band minimum, respectively

atomically abrupt junctions and is explained by (metal) induced gap states, which have first been introduced by Heine [9]. They are the result of wave function matching at the interface and are clearly illustrated by electronic structure calculations [10]. Fermi level pinning is reported to be less strong for polar-bonded materials as oxides [2, 11]. However, the experimental basis concerning barrier heights at oxide semiconductor interfaces is rather limited and is mostly restricted to electrical measurements. Electrical determinations of barrier heights on ZnO are, e.g., presented in Chap. 7 of this book. Other reviews are given in [12, 13].

The issue of Schottky barrier formation to ZnO is not treated in this chapter as such contacts are not of big importance in thin-film solar cells. This is related to the fact that in thin film solar cells metals are only used to contact highly-doped films. For degenerately doped semiconductors, the barrier heights become very small because of the large space charge associated with depletion layers in such materials.

4.1.2 ZnO in Thin-Film Solar Cells

Compared with the interfaces illustrated in Fig. 4.1, the role played by ZnO in a $Cu(In,Ga)Se_2$ thin-film solar cell is considerably more complex (see also Chap. 9). The basic structure and the commonly used energy band diagram are shown in Fig. 4.2 [14]. It is evident that ZnO does not only provide a transparent contact, but is also an essential part of the p/n-junction of the device. Best solar cells with efficiencies of almost 20 % are achieved if a ZnO bilayer is used, which consists of a combination of a nominally undoped ZnO and a highly doped ZnO layer [15]. ZnO is deposited onto a CdS layer, which is prepared mostly by a chemical bath. The lattice constants of CdS are significantly larger than those of ZnO leading to a strongly lattice mismatched system. At such an interface, crystallographic defects are unavoidable.

The electronic defect states associated with such defects typically have energy positions within the band gap of the smaller gap semiconductor and

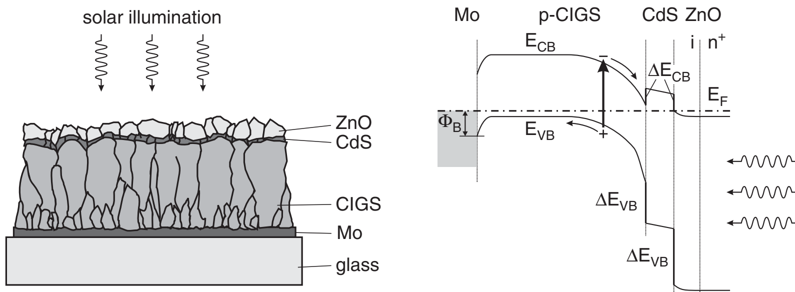

Fig. 4.2. Structure and energy band diagram of a $Cu(In,Ga)Se_2$ (CIGS) thin-film solar cell. The ZnO window layer typically consists of a combination of a nominally undoped ZnO and a highly doped ZnO layer

can be electrically charged. They might act as carrier recombination centers but will also modify the electrical potential distribution. Another significant difference of the interface of ZnO in the Cu(In,Ga)Se_2 solar cell compared with conventional semiconductor systems lies in the fact that the ZnO layer is typically prepared by magnetron sputtering. This is partially dictated by technological requirements (fast and large area coating) but also due to advantages of the technique that allows to prepare highly doped films at low substrate temperature (see Chaps. 2 and 5). The latter issues are particularly related to the energetic particles involved in sputter deposition. However, it is generally believed that these energetic particles lead to a damage of the substrate surface by introducing defects. Avoiding such a sputter damage of the Cu(In,Ga)Se_2 semiconductor might, e.g., explain why a CdS buffer layer is necessary to achieve highest conversion efficiencies. However, no clear evidence for the influence of sputter damage has been presented so far.

A less complex situation is present if ZnO films are used as substrates for amorphous Si thin-film solar cells. These are described in chapters 8 and 6 of this book. In this case the problem of possible sputter damage and, due to the amorphous nature of the semiconductor, also of lattice mismatch are not an issue. For thin film silicon solar cells, light trapping is of particular interest. This requires a dedicated surface morphology, which can be either achieved directly by depositing the ZnO layer using chemical vapor deposition (see Chap. 6) or by a suitable etching process of sputter deposited films as described in Chap. 8 of this book. The morphology obtained by etching is strongly dependent on the sputter deposition parameters. It is well known that etching of semiconductors is highly anisotropic and depends on surface orientation and termination [16, 17]. Thus, the surface properties of sputter deposited ZnO films are also of importance for thin film silicon solar cell devices.

4.1.3 Photoelectron Spectroscopy (PES)

Electronic properties of semiconductor surfaces and interfaces can be probed by different techniques, including scanning probe techniques [18, 19], Kelvin probe [20] and photoelectric yield [21] measurements, electrical techniques such as current–voltage and capacitance–voltage measurements [1, 12, 13, 22], DLTS[2] and admittance spectroscopy [23–27], internal photoemission [8, 22, 28], cathodoluminescence [29, 30], and others. A versatile tool that has contributed significantly to the understanding of semiconductor interfaces is X-ray and ultraviolet photoelectron spectroscopy (XPS and UPS). Both most frequently used (standard) applications of photoelectron spectroscopy are elemental and chemical surface analysis [31, 32]. Binding energies in photoelectron spectroscopy (PES) are measured with respect to the Fermi level. Since samples are electrically connected to the spectrometer

[2] Deep level transient spectroscopy.

system, the Fermi level is at a constant energy, which can be determined by a calibration measurement using a metallic sample. This allows to observe changes of the Fermi level within the band gap. If, for a given sample, the binding energy of a core level (CL) is known with respect to the valence band maximum ($BE_{VB}(CL)$), the core-level binding energy itself can be directly used as a measure for the position of the Fermi level in the band gap ($E_F - E_{VB} = BE(VB)$).

During an interface experiment, an overlayer is stepwise deposited onto a substrate. By monitoring the substrate and overlayer core-level binding energies during deposition, the evolution of the valence band maxima of the substrate and of the overlayer can be followed during interface formation [33–36]. The procedure is outlined in Fig. 4.3. As will be shown in Sects. 4.2.3.3 and 4.3.3, care has to be taken when applying this standard procedure to study surfaces and interfaces of sputter-deposited ZnO films, as $BE_{VB}(CL)$ depends on the deposition parameters for this material.

Photoelectron spectroscopy is a highly surface sensitive technique because of the inelastic mean free path of the photoelectrons λ_e, which depends on the electron kinetic energy E_{kin} and has typical values of 0.2–3 nm [31,37,38]. Determination of Schottky barrier heights Φ_B, or valence band discontinuities ΔE_{VB}, can be performed by following the evolution of the position of the valence band maxima with respect to the Fermi level of substrate and overlayer with increasing thickness of the overlayer. For layer-by-layer growth the attenuation of the substrate intensities is given by the inelastic

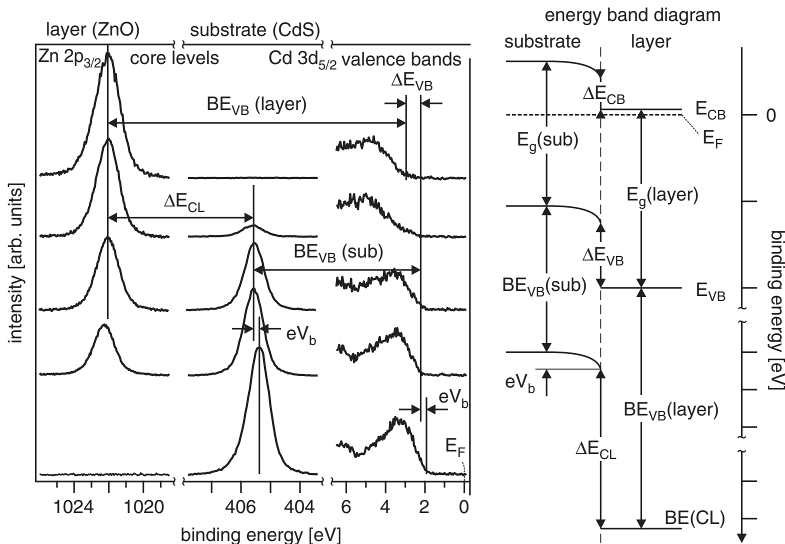

Fig. 4.3. Experimental procedure for the determination of the band alignment using photoelectron spectroscopy

mean free path of the photoelectrons. Hence, after a film thickness of ∼5 nm, the substrate emissions are completely extinguished. The study of interface formation with PES thus requires control of the film thickness in the subnanometer range. The rapid contamination of surfaces in air requires that the sample transfer between surface preparation or film deposition to the photoelectron spectrometer is performed in vacuum. Consequently, the analysis system has to *integrate* all required thin film preparation chambers and a surface analysis tool. The layout of such a system as it is used in Darmstadt is shown in Fig. 4.4.

Experimental determinations of barrier heights on oxide semiconductor interfaces using photoelectron spectroscopy are rarely found in literature and no systematic data on interface chemistry and barrier formation on any oxide are available. So far, most of the semiconductor interface studies by photoelectron spectroscopy deal with interfaces with well-defined substrate surfaces and film structures. Mostly single crystal substrates and, in the case of semiconductor heterojunctions, lattice matched interfaces are investigated. Furthermore, highly controllable deposition techniques (typically molecular beam epitaxy) are applied, which lead to films and interfaces with well-known structure and composition. The results described in the following therefore, for the first time, provide information about interfaces with oxide semiconductors and about interfaces with sputter-deposited materials. Despite the rather complex situation, photoelectron spectroscopy studies of sputter-deposited

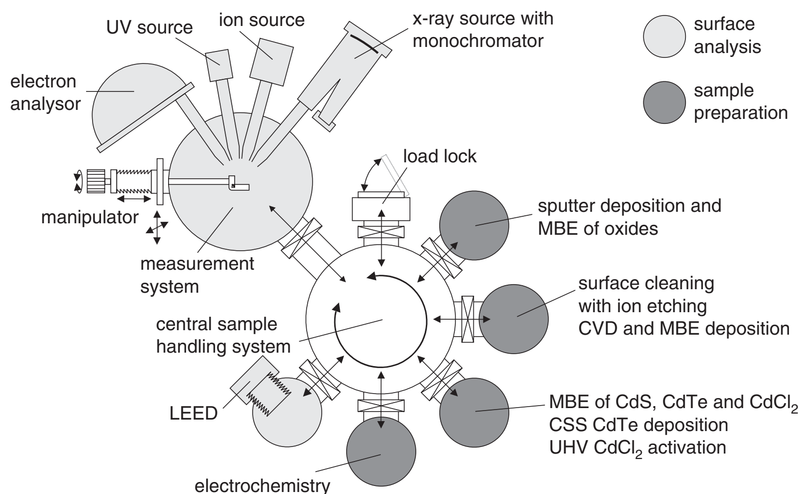

Fig. 4.4. Layout of the integrated surface analysis and preparation system DAISY-MAT (Darmstadt integrated system for materials research). A photoelectron spectrometer is connected by a sample handling system to various deposition and surface treatment chambers. Preparation and analysis can be repeatedly performed under controlled ultrahigh vacuum conditions

ZnO films can provide substantial information on chemical and electronic properties of ZnO surfaces and interfaces, which occur in real thin film solar cell structures. In addition, general information on the interface formation of oxide materials can be extracted. In the following we describe:

– Electronic surface properties including Fermi level positions, work functions, and ionization potentials of sputter-deposited ZnO and Al-doped ZnO films in dependence on deposition parameters. The results provide insight into aspects of doping, surface chemistry, and terminations.
– Interfaces of sputter-deposited ZnO and ZnO:Al films with different substrate materials (CdS, In_2S_3, and $Cu(In,Ga)Se_2$) in dependence on deposition parameters. The band alignments and chemical interactions at the interfaces are discussed.

4.2 Surface Properties of ZnO

4.2.1 Crystallographic Structure of ZnO Surfaces

The wurtzite lattice of ZnO and its low-index surfaces are shown in Fig. 4.5. The basic low index surface terminations are (0001), $(000\bar{1})$, $(10\bar{1}0)$, and $(11\bar{2}0)$. The (0001) and $(000\bar{1})$ represent the zinc and oxygen-terminated surfaces of the polar {0001} direction, which corresponds to the {111} direction of the cubic zincblende lattice. In contrast to the polar (100) and $(\bar{1}00)$ surfaces of the zincblende lattice, the surfaces with threefold symmetry (111)

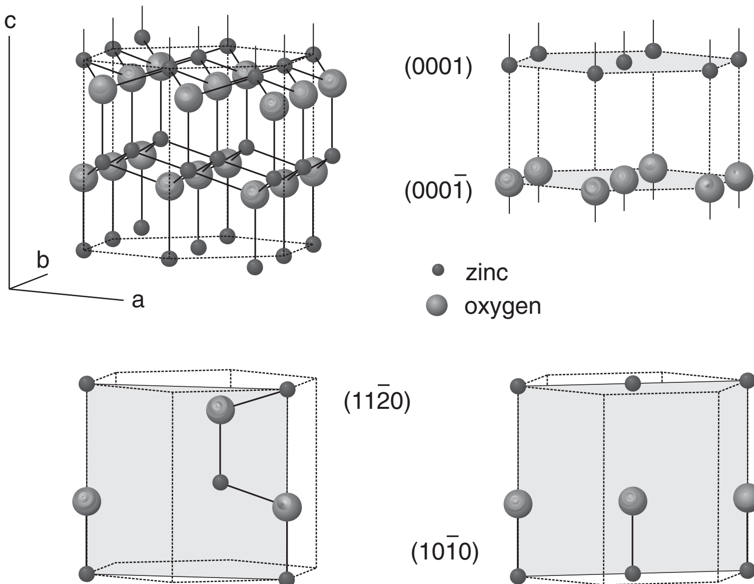

Fig. 4.5. Crystallographic structure of ZnO and its basic surfaces

and $(\bar{1}\bar{1}\bar{1})$ are not equivalent. There is thus a clear distinction between the two surfaces. The same is true for the basal plane (0001) and $(000\bar{1})$ surfaces of the wurtzite lattice. These are important surface terminations for sputtered ZnO thin films, which often grow with a (0001) texture (see e.g., [39] and other contributions to this book). The $(10\bar{1}0)$ and $(11\bar{2}0)$ surfaces are nonpolar, i.e., they contain the same number of zinc and oxygen atoms. These surfaces show no reconstruction [40, 41]. The wurtzite $(11\bar{2}0)$ surface directly corresponds to the well-known nonpolar (110) surface of the zincblende lattice [42].

Surfaces of real crystals never adopt the bulk-truncated structures shown in Fig. 4.5. They reconstruct or relax (inwards or outward movement of the atoms) to minimize their surface energy [42]. Known surface structures of zincblende and wurtzite structure semiconductors are summarized in [43]. Nonpolar surfaces of wurtzite $(11\bar{2}0)$ and $(10\bar{1}0)$ surfaces show no lateral surface reconstructions and are supposed to have a structure similar to the well-known zincblende (110) surface, which is characterized by an inward relaxation of the surface cations and partial electron transfer from the surface cation dangling bond to the surface anion dangling bond [42, 43].

Polar surfaces of semiconductors cannot be bulk-truncated because of the alternating charge of atomic planes in polar directions, which will lead to a diverging electrostatic potential due to the large number of lattice planes [44]. Compensation of the diverging electrostatic potential is possible by a rearrangement of charges at the surface. For the basal (0001) and $(000\bar{1})$ surfaces of ZnO this corresponds to a removal of $\sim 1/4$ of the surface charge.[3] In principle, the rearrangement of the charge can be achieved by: (1) creation of a metallic surface by introduction of surface states; (2) removal of surface atoms; and (3) charged impurities at the surface, as e.g. hydroxyl or hydroxide species. All mechanisms have been invoked for the basal surfaces of ZnO [45–49].

The uncertainty concerning the identification of the stabilization mechanism on polar ZnO surfaces is partly due to the lack of atomically resolved STM images. Such images are possible for the nonpolar $(10\bar{1}0)$ and $(11\bar{2}0)$ surfaces [40, 41] but have, to our knowledge, not been reported for polar surfaces. The polar cation terminated (111) surface of zincblende compounds typically displays a 2×2 reconstruction associated with removal of every fourth surface cation [43, 50–52]. This structure is ideally suited to match the charging condition for surface stabilization for this particular surface orientation. The 2×2 reconstruction and the missing surface atoms can directly be observed by STM [52]. In contrast to literature [53], a 2×2 reconstruction is also frequently observed in our group for the (0001) surface of wurtzite CdS.[4] The reconstruction on the anion terminated $(\bar{1}\bar{1}\bar{1})$ surfaces of III–V and II–VI zincblende compounds are considerably more complex. These surfaces

[3] The factor of 1/4 results from the distance of the Zn and O lattice planes along the *c*-direction.

[4] B. Siepchen et al., Darmstadt University of Technology (unpublished results).

show a strong tendency for facet formation [43]. Nonfacetted GaAs($\bar{1}\bar{1}\bar{1}$) show complex superstructures associated with adsorbed As species [54].

In contrast to most of the zincblende and wurtzite materials, the ZnO (0001) and (000$\bar{1}$) surfaces are usually not reconstructed [40,47]. Only Kunat et al. report the observation of a 1×3 reconstruction for the ZnO (000$\bar{1}$) surface and attribute the unreconstructed surface to a hydrogen termination [49]. A new stabilization mechanism for polar ZnO (0001) surfaces has been introduced by Dulub et al. based on scanning tunneling microscopy [41,45, 46]. This involves a large number of oxygen-terminated step edges on the Zn-terminated surface. This termination allows for field compensation and is consistent with an unreconstructed surface and with the predominant Zn surface atoms found in low energy ion scattering (LEIS) [40].

4.2.2 Chemical Surface Composition of Sputtered ZnO Films

Examples of XPS spectra recorded from in situ sputter-deposited ZnO and ZnO:Al films are shown in Fig. 4.6. Absence of contaminations is evident from the survey spectra, which show only emissions from Zn and O. Aluminium-doped ZnO films, deposited from a target with a nominal Al concentration of 2 wt %, also show a small Al signal. Detailed spectra of the Zn $2p_{3/2}$, O 1s, Zn LMM Auger, and valence band emissions for largely different deposition conditions are given in the lower half of Fig. 4.6.

Despite the strongly varying deposition conditions of the films shown in Fig. 4.6, all spectra represent the ZnO composition. Binding energy variations are largely due to changes of the Fermi level position (see Sect. 4.2.3.1). The O 1s and the Zn LMM Auger line show a noticeably different shape for the most highly doped films, which are those deposited from ZnO:Al targets without addition of oxygen to the sputter gas. The high doping level is reflected by the highest binding energy of the corresponding spectra. The different shapes of the Zn LMM line can be explained by the changes in electron concentration: The electron gas in highly degenerate TCOs leads to screening of the core hole and to inelastic scattering of the photoelectron because of excitation of plasmons (see Fig. 4.17) [55–58]. The latter leads to shoulders on the high binding energy side of the core levels and to a second Auger emission, which is shifted to lower binding energies [55]. This explains the typical "smeared" appearance of the Zn LMM Auger spectra of the film with the highest carrier concentration (spectra (d) in Fig. 4.6).

4.2.2.1 Oxygen and Aluminium Content

The chemical composition of the surface can be evaluated from the integrated intensities of the core-level emissions [31]. Unfortunately, the accuracy of quantitative analysis with photoelectron spectroscopy is generally limited to a few percent even when good standards are available [31]. Therefore, even from a large number of measured samples it was not possible to observe a

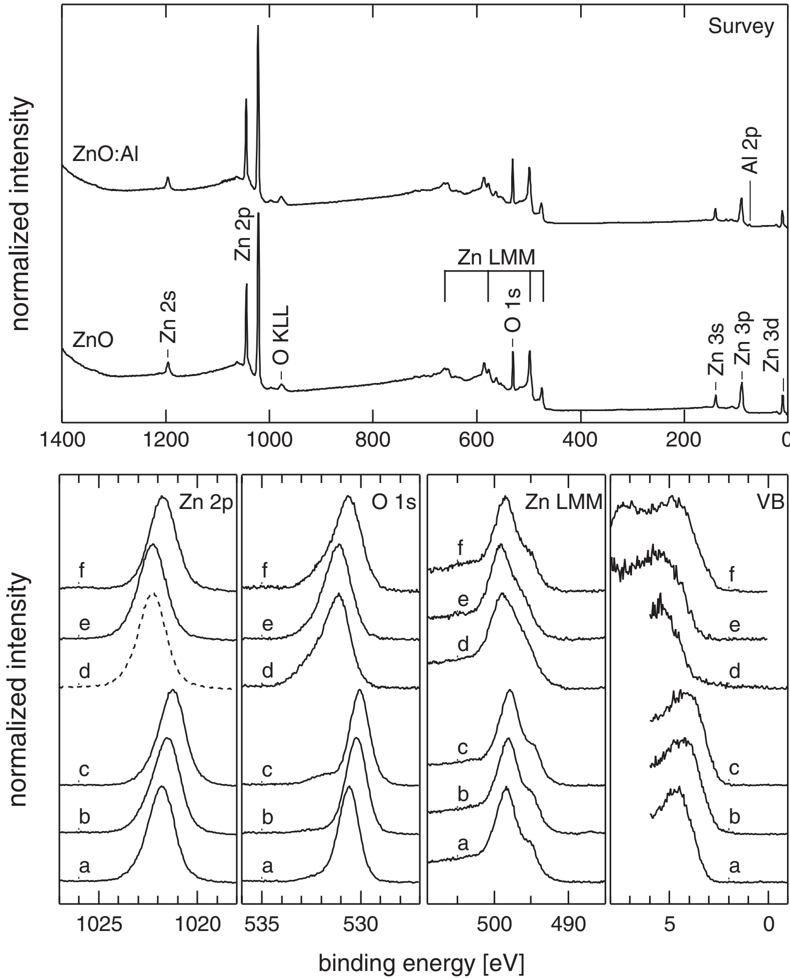

Fig. 4.6. X-ray photoelectron spectra of undoped ZnO (**a**–**c**) and of Al-doped ZnO (**d**–**f**) prepared by magnetron sputtering. The spectra are excited with monochromatic Al Kα radiation ($h\nu = 1486.6$ eV). ZnO:Al films are prepared from a target containing 2 wt % Al. The films are prepared with 100 % Argon as sputter gas either at room temperature (**a** and **d**) or at a substrate temperature of 400°C (**b** and **e**). Spectra (**c**) and (**f**) are recorded from films deposited onto samples held at room temperature in a sputter gas mixture of 50 % argon and 50 % oxygen

systematic variation of the oxygen to zinc intensity ratio in dependence on deposition conditions. The oxygen content in films deposited from undoped ZnO targets varies between 46 and 49 %. Sensitivity factors supplied by the manufacturer of the XPS system[5] are used for quantification. Nonappropriate

[5] Physical Electronics: PHI 5700.

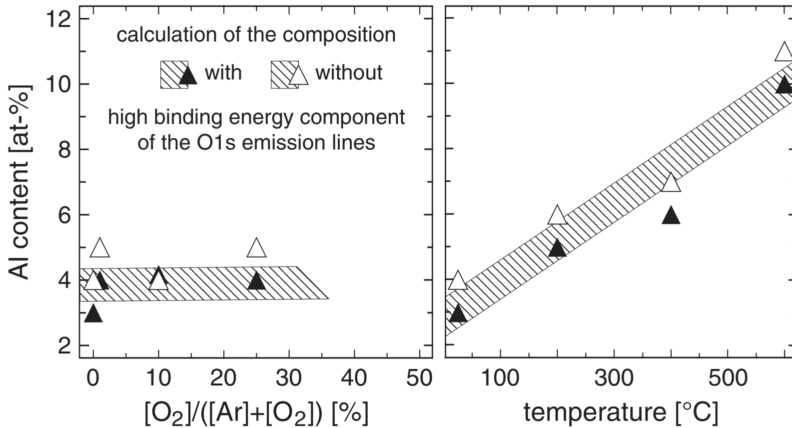

Fig. 4.7. Aluminium content of sputter deposited ZnO:Al films. A target with a nominal Al content of 2 wt % has been used. The *shadowed regions* indicate the general behavior. The atomic concentration is calculated with and without considering the high binding energy oxygen species, which contributes to the O 1s signal (see Sect. 4.2.2.2)

sensitivity factors are most likely the reason for the deviation of the determined composition from the nominal oxygen content of 50 %. Even larger deviations are observed for other oxides. It is thus not possible to derive an absolute number for the composition of the films.

A better reproducibility and quantification of concentrations with XPS is possible for the relative cation concentrations of mixed cation systems as e.g. (Zn,Al)O, (Zn,Mg)O [59], and (In,Sn)O (ITO) [58]. Figure 4.7 shows the variation of the Al content of ZnO:Al films deposited with different Ar/O_2 ratios in the sputter gas and at different substrate temperatures. There is only a small or negligible dependence of the Al content if oxygen is added to the sputter gas. In contrast, a strong enrichment of Al is obtained at higher substrate temperature. This is explained by the high vapor pressure of Zn, which reevaporates from the surface at higher substrate temperatures before a ZnO compound can form. A comparable behavior has been observed for (Zn,Mg)O films, where also a strong enrichment of Mg is observed at higher substrate temperatures [59].

4.2.2.2 Oxygen-Related Surface Species and Initial Growth of ZnO Films

The O 1s spectra in Fig. 4.6 show an additional small emission at higher binding energies. The energy difference between the ZnO-related emission at 530–531 eV and the high binding energy component amounts to 1.6–1.8 eV. Such a species is always observed on ZnO surfaces. In literature, it is mostly attributed to adsorbed species. These include water and hydroxides

[49, 60–62], physisorbed or chemisorbed oxygen [63–66], and CO_x species (see [67] and references therein). The latter can be excluded as an explanation for the species observed here because of the absence of carbon. Chen et al. also mention a possible contribution of oxygen vacancies [68] and Stucki et al. suggest that the high binding energy oxygen species is related to oxygen interstitials [69].

ZnO is rather hygroscopic. It is, therefore, reasonable to expect hydroxide at the surfaces of samples that have been exposed to air. Even for in situ sputter-deposited films, hydroxide species cannot be excluded since water and hydrogen is always present in the residual gas, in the ceramic ZnO target, and/or the sputter gas. However, a high binding energy O 1s component is also observed at UHV-cleaned single crystal ZnO surfaces [49] and is still present after heating in UHV to >500°C [49, 70].

The high binding energy O 1s component of in situ sputter-deposited ZnO films is related to a surface species. Photoelectron spectra recorded with different photon energies at the synchrotron are shown in Fig. 4.8. Because of the different photon energies, the photoelectrons have different kinetic energies, which results in different photoelectron escape depths. The highest surface sensitivity is obtained for a photoelectron kinetic energy of ∼50 eV, which is obtained for an excitation energy of 580 eV. With increasing surface

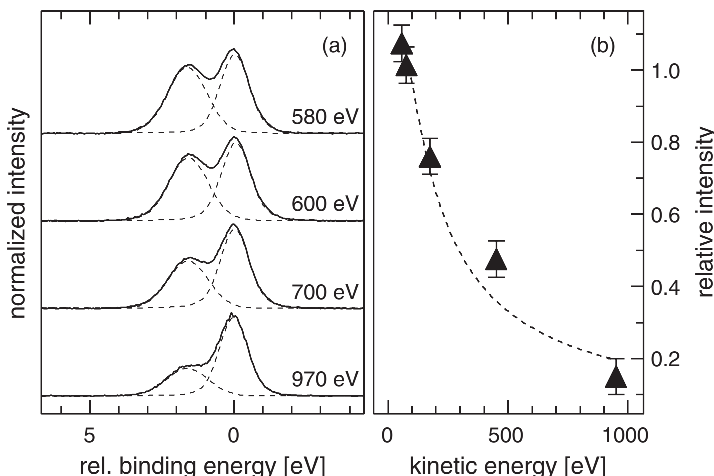

Fig. 4.8. (**a**) O 1s core-level spectra of a sputter-deposited undoped ZnO film. The spectra were recorded with different photon energies at the synchrotron. Binding energies are given with respect to the ZnO component. The relative intensity of the high binding energy component is shown in (**b**). The *dashed line* represents the calculated dependency for a homogeneous surface layer using energy-dependent inelastic mean paths as provided by Tanuma, Powell, and Penn [37]. Using their material parameters for ZnS, the fit to the experimental data reveals a thickness of the surface layer of 3.3 ± 0.1 Å

sensitivity, the contribution of the high binding energy component to the total O 1s intensity increases. The intensity ratio of the high binding energy to the ZnO component of the O 1s level is shown in Fig. 4.8b. The dependence on electron kinetic energy is reasonably well reproduced by modeling the intensity ratio using a homogeneous surface layer with a different oxygen species. The formula for the inelastic mean free path proposed by Tanuma, Powell, and Penn with the parameters for ZnS [37] has been used to calculate the curve. Fitting the model for the intensity to the experimental data reveals a thickness of the surface layer of 3.3 ± 0.1 Å. The different oxygen component is, therefore, located mostly in the topmost surface layer.

Observations made during the deposition of ZnO on different substrate surfaces support this model and provide arguments for the chemical identification of the surface oxygen species. This is illustrated in Fig. 4.9. The spectra show the evolution of the O 1s signal during stepwise deposition of ZnO or ZnO:Al onto CdS, In_2S_3 and $Cu(In,Ga)Se_2$ by dc magnetron sputtering. The growth is interrupted several times in order to follow the changes in the spectra with ZnO thickness. During deposition onto CdS, the high binding energy component dominates at low coverage over the ZnO component. It is reduced during further deposition until it reaches the intensity typically observed for thick ZnO films. Although the O 1s spectra of ZnO and ZnO:Al are different due to the different free carrier concentrations, the behavior is

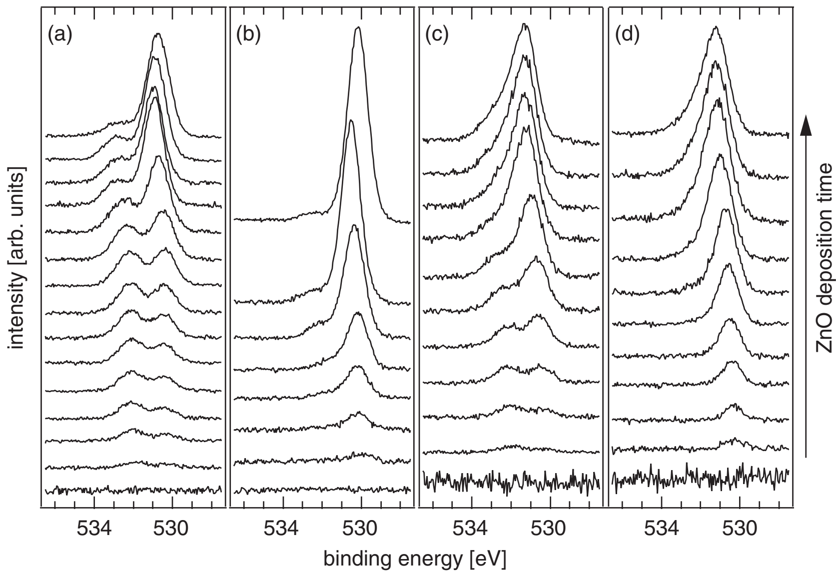

Fig. 4.9. O 1s spectra recorded during stepwise deposition of ZnO (**a** and **b**) or ZnO:Al (**c** and **d**) onto different substrates. The surface species dominates at low coverage for CdS substrates (**a** and **c**). For $Cu(In,Ga)Se_2$ (**b**) or In_2S_3 (**d**) substrates the surface species occurs not until a thick ZnO film is deposited

the same for both interfaces. Also alloying of Mg with ZnO results in an identical evolution of the O 1s spectra [71].

A different behavior is observed during deposition onto In_2S_3 or CIGS (see Fig. 4.9c,d). At low coverage the high binding energy component is not present, although the deposition conditions are otherwise identical. The substrate, therefore, determines whether the high binding energy component is observed or not at low coverage. It is thus not likely that the surface component is due to a hydroxide species originating from a contamination of the deposition system, as this is the same in all cases. It is rather suggested that the surface component is related to a peroxide species. In a peroxide, the O^{2-} ions are replaced by O_2^{2-} ions. The situation resembles the dumbbell-like oxygen interstitial defect recently described in literature [72, 73] (see also Sect. 1.6 of this book).

The presence of peroxide species at ZnO surfaces is not unreasonable. During deposition the surface is exposed mainly to Zn and O_2 species. There are also other, more reactive, oxygen species in the gas phase. However, the percentage of dissociated and ionized gas species in a magnetron discharge is below 1 % [74] (a detailed description of sputter deposition of ZnO is given in Chap. 5 of this book). The growth of the oxide film, therefore, requires dissociation of the O_2 species. According to the spectra shown in Fig. 4.9 it is suggested that oxygen dissociation is not favorable on the surfaces of the II–VI compounds ZnO and CdS, while $Cu(In,Ga)Se_2$ and In_2S_3 obviously favor the dissociation of oxygen molecules. The different behavior is summarized in a tentative model in Fig. 4.10.

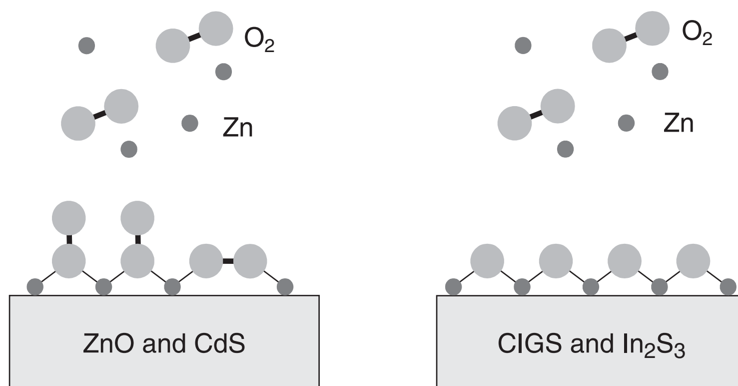

Fig. 4.10. Tentative model describing the initial growth of ZnO on different substrates that is consistent with the different evolution of the O 1s signal (Fig. 4.9) and the different reactivitiy at the interface (see Sects. 4.3.2.1, 4.4.1, and 4.5.2). A peroxo-like surface species is observed during growth on ZnO and CdS substrates but not on In_2S_3 and $Cu(In,Ga)Se_2$ substrates. The differences are attributed to the abilities of the surfaces to dissociate the adsorbed O_2 molecules

4.2.3 Electronic Structure of ZnO Surfaces

The electronic potentials at a semiconductor surface are shown in Fig. 4.11. There are basically two independent quantities that can be determined using photoelectron spectroscopy: The distance between the Fermi energy and the valence band maximum (BE(VB) = $E_{\mathrm{F}} - E_{\mathrm{VB}}$) and the work function (ϕ). The former quantity can change with doping and surface band bending, which is introduced by charged surface or interface states. A change of the surface Fermi level position changes the work function by the same amount. A change in work function can also be induced by changes of the surface dipole of the material by a modification of the structure of the surface or by adsorbates [75].

Motivated by the application of ZnO in gas sensors and catalysis and by the more general desire to understand surface properties of ionically bonded solids, electronic properties of ZnO surfaces have been investigated for many years [20, 76–80]. An overview of the early work on ZnO surface properties is included in the book of Henrich and Cox [81].

An extensive investigation of the surface potentials at ZnO (0001), (000$\bar{1}$), and (10$\bar{1}$0) surfaces using UPS is described by Jacobi et al. [79]. A noticeable change of Fermi level position after surface preparation (ion bombardment and annealing in vacuum) is observed with time for the oxygen terminated (000$\bar{1}$) and to a lesser extend also for the nonpolar (10$\bar{1}$0) surface. These changes in band bending have been related to oxygen removal caused by UV irradiation. The Fermi level stabilizes after several hours close to the

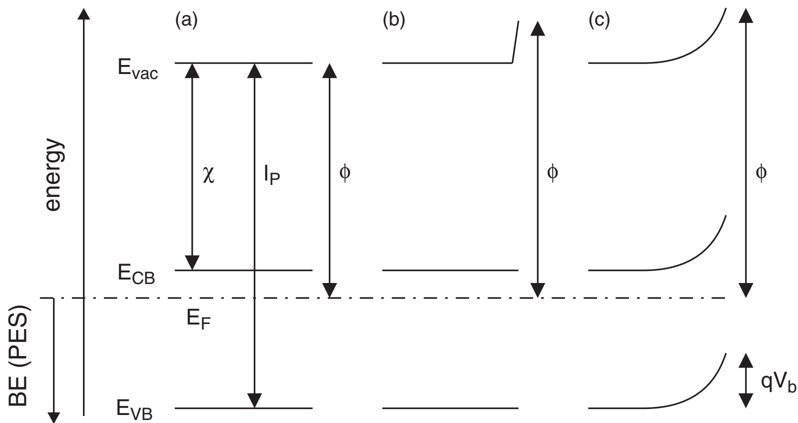

Fig. 4.11. Surface potentials of an n-type semiconductor in flat band condition (**a**). The work function ϕ can change either by modification of the surface dipole preserving flat bands but modifying the electron affinity χ and ionization energy $I_{\mathrm{P}} = \chi + E_{\mathrm{g}}$ (**b**). The work function might also change by bending of the bands at the surface qV_{b} (**c**). Surface dipole and band bending could also change simultaneously. In photoelectron spectroscopy, binding energies are measured with respect to the Fermi energy

conduction band minimum. For the (0001) surface termination, the Fermi level is close to the conduction band minimum directly after surface preparation (ion bombardment and annealing). In addition, a time-dependent reduction of work function is observed for all surface orientations. A similar effect has also been reported by Moormann et al. [20, 77].

More recently, Meier has also observed time-dependent binding energy shifts of ZnO thin films [82]. The shifts observed after heating magnetron-sputtered ZnO thin films are in the same direction and of the same magnitude as those described by Jacobi et al. In addition, Meier describes also binding energy shifts in the opposite direction, directly after deposition at low substrate temperatures. The shifts are related to changes in hydrogen and hydroxide concentrations near the surface [82]. In our studies, we have not observed time-dependent binding energies of the sputter-deposited ZnO films. A possible reason for the difference might be the different surface termination of the films. As will be shown below, the ZnO films used in this study were prepared by dc magnetron sputtering and show mainly a (0001) surface termination. For this particular surface orientation no changes in surface Fermi level position with time have been observed by Jacobi et al. [79]. The ZnO films investigated by Meier et al. were deposited by rf magnetron sputtering [82], which might lead to a different surface termination.

4.2.3.1 Surface Fermi Level Position

The core and valence levels in Fig. 4.6 show comparable binding energy shifts in dependence on deposition conditions. The shifts are mainly due to shifts of the Fermi level position at the surface. The Fermi level position with respect to the valence band maximum is directly measured as the binding energy of the valence band maximum. Values for magnetron-sputtered ZnO and ZnO:Al thin films are shown in Fig. 4.12 in dependence on oxygen content in the sputter gas and substrate temperature.

Films deposited from the undoped and Al-doped target at room temperature without addition of oxygen to the sputter gas show a valence band maximum $\sim$2.8 and $\sim$3.7 eV below the Fermi energy, respectively. If we take the band gap of ZnO as 3.3 eV, the surface Fermi level of highly doped ZnO:Al is above the conduction band minimum, as expected for a degenerately doped n-type semiconductor. A Fermi level position $\sim$0.4 eV above the conduction band minimum is in good agreement with observed shifts of the optical transitions in ZnO because of filling of conduction band states, known as Burstein–Moss shift [83, 84]. Therefore, for degenerately doped ZnO:Al, the surface Fermi level position detected by XPS/UPS agrees with the bulk Fermi level position detected by optical measurements, which corresponds to the flat band situation shown in Fig. 4.11a. This indicates that the ZnO surfaces are free of surface states in the fundamental band gap, in agreement with theoretical calculations of the electronic structure of ZnO surfaces [85]. Surface-sensitive electron energy loss spectroscopy (EELS) also indicates the

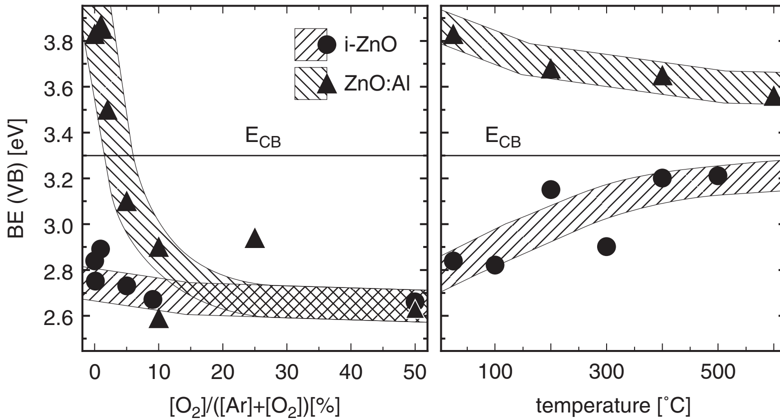

Fig. 4.12. Valence band maximum binding energies of magnetron sputtered ZnO and ZnO:Al films in dependence on the oxygen content in the sputter gas at room temperature (*left*) and in dependence on substrate temperature for deposition in pure Ar (*right*). The binding energies are derived from X-ray excited valence band spectra. All films were deposited using a total pressure of 0.5 Pa, a sputter power density of 0.74 W cm^{-2} and a substrate to target distance of 10 cm. The *horizontal line* indicates the position of the conduction band minimum

absence of electronic transitions with energies below the fundamental gap at different surfaces [86]. The theoretical and the EELS investigations were performed on different polar and nonpolar single crystal surfaces. Obviously, the results are also valid for polycrystalline sputtered ZnO films.

The absence of surface states in the fundamental gap allows to discuss the measured Fermi level positions in Fig. 4.12 in terms of bulk doping. This is particularly interesting for the addition of oxygen to the sputter gas. Addition of oxygen to the sputter gas does not change the Fermi level for the undoped material, but it leads to a considerable lowering of the Fermi level for films deposited from the Al-doped target. The latter compares well with the reported reduction of conductivity of ZnO:Al films with the addition of oxygen (see e.g., [87]). The origin of the reduced carrier concentration and the associated lowering of the Fermi level is not clear yet. It has been argued that addition of oxygen leads to an increased formation of Al_2O_3 [87], thus removing Al atoms from the active dopant sites, which are provided by the regular Zn lattice sites (Al_{Zn}). However, a reduced carrier concentration can also result from an increased compensation because of the introduction of intrinsic acceptor states. According to recent theoretical calculations, zinc vacancies or oxygen interstitials in a dumbbell or rotated dumbbell configuration are possible candidates (see e.g., [72, 73] and Sect. 1.6). The refined calculations indicate that the zinc vacancy has the lowest formation energy under oxygen-rich conditions [73]. In a recent publication by Lany and Zunger [S. Lany, A. Zunger, Phys. Rev. Lett. 98, 045501 (2007)], the zinc vacancy

has been explicitly used to demonstrate the compensation mechanism with increasing oxygen partial pressure (see Fig. 1.15 in Sect. 1.6.1). However, this consideration holds for thermodynamic equilibrium while the deposition of ZnO by magnetron sputtering is far from equilibrium and also includes energetic particles. Therefore, also other defects will be present. In any case, the situation is again different compared with ITO, where it is well accepted that the formation of neutral ($2\,Sn_{In}O_i$) defect complexes is responsible for the reduction of conductivity under oxidizing conditions [88, 89].

For higher oxygen content in the sputter gas, the Fermi level stabilizes at ∼2.7 eV above the valence band maximum. This particular energy position seems to be related to an intrinsic defect level of ZnO. A similar Fermi level position has also been observed during interface experiments [90]. For a Fermi level position ∼0.6 eV below the conduction band, it can be expected that all Al_{Zn} donors are ionized. In principle, the Fermi level stabilization energy should then be a few kT lower than the energy level of an acceptor state, such that a considerable fraction of the acceptors are ionized. However, the identification of the associated defect level is not straightforward, as direct experimental observations of intrinsic defect energy levels are, in most cases, not available. On the other hand, theoretical calculations can reveal defect levels but suffer from an incorrect determination of band gaps (see e.g., discussion in [73]). Within this uncertainty, both the zinc vacancy and the oxygen interstitials are, according to density functional theory calculations, reasonable candidates for the observed Fermi level stabilization energy under oxygen-rich conditions [73]. Both defects form rather deep acceptor states.

4.2.3.2 Work Function and Ionization Potential

The work functions and ionization potentials of sputter-deposited ZnO and ZnO:Al films are shown in Fig. 4.13. The different Fermi level positions of ZnO and ZnO:Al for deposition at room temperature in pure Ar are also observed in the work function. The undoped films prepared under these conditions have a work function of ∼4.1 eV, while the Al-doped films show values of ∼3.2 eV. The difference is almost of the same magnitude as for the Fermi level position and, therefore, explained by the different doping level. Also the ionization potentials are almost the same under these preparation conditions. The work function of the undoped material is close to the value reported by Moormann et al. for the vacuum-cleaved Zn-terminated (0001) surface [20]. The same authors report a work function of 4.95 eV for the oxygen terminated ZnO$(000\bar{1})$ surface, which is in good agreement with the values obtained for films deposited with $\gtrsim$5 % oxygen in the sputter gas. Since the Fermi level position of the undoped ZnO films does not depend on the oxygen content in the sputter gas (Fig. 4.12), the different work functions correspond to different ionization potentials.

The ionization potentials of the undoped ZnO films prepared at room temperature are ∼6.9 eV for films deposited in pure Argon and raise to ∼7.7 eV

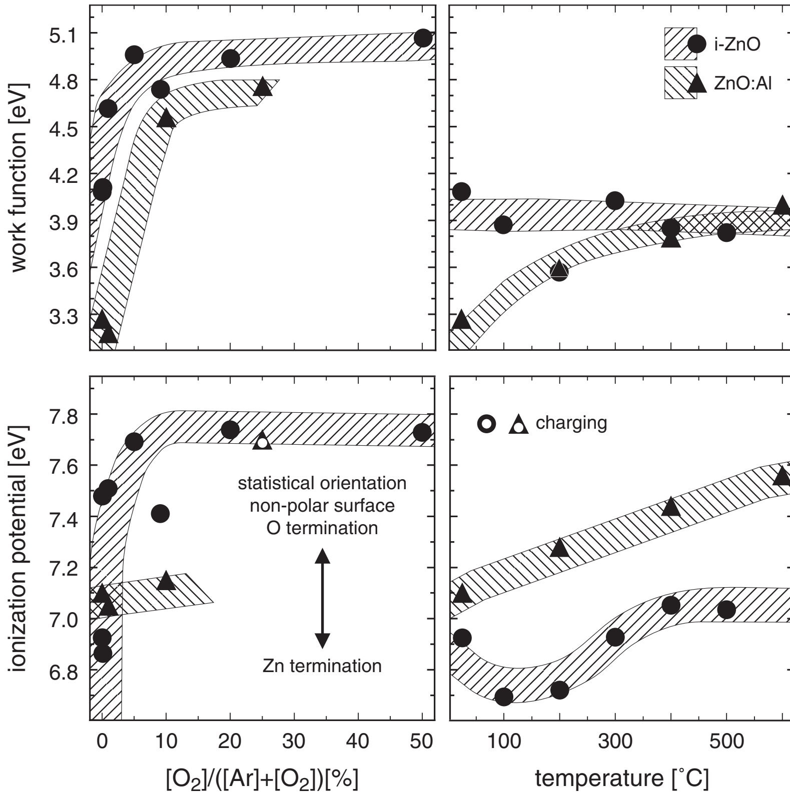

Fig. 4.13. Work function and ionization potential of magnetron sputtered ZnO and ZnO:Al films in dependence on oxygen content in the sputter gas for samples deposited at room temperature (*left*) and in dependence on substrate temperature for deposition in pure Ar (*right*). The values are derived from He I excited valence band spectra. All films were deposited using a total pressure of 0.5 Pa, a sputter power density of 0.74 W cm^{-2} and a substrate to target distance of 10 cm

for films deposited with $\gtrsim$5 % oxygen in the sputter gas. The lower value corresponds well with literature data given for the electron affinity of ZnO(0001) (3.7 eV) [79]. Ionization potentials of ~7.82 eV have been determined by Swank et al. for the nonpolar ZnO($10\bar{1}0$) surface [76] as well as by Jacobi et al. for ZnO($10\bar{1}0$) and for oxygen terminated ZnO($000\bar{1}$). These values are in good agreement with the ionization potential of ZnO films sputtered from the undoped target with more than 5 % oxygen in the sputter gas.

The variation of the ionization potential with surface orientation evident from the literature data corresponds well with a systematic study by Ranke using a cylindrical GaAs single crystal [91]. This revealed that the electron affinity of the cation terminated (111) surface of GaAs (corresponding to wurtzite (0001)) is 0.4–0.5 eV lower than those of other surface terminations. The same variation is observed at single crystal surfaces of CdTe and

CdS [92]. The ionization potentials of CdTe(111), $(\bar{1}\bar{1}\bar{1})$, and (110) amount to 5.3, 5.6, and 5.65 eV, those of epitaxial CdS films deposited onto these surfaces are given by 6.25, 6.85, and 6.75 eV, respectively. For comparison, the ionization potentials of polycrystalline CdTe and CdS films amount to 5.8 and 6.9 eV [92]. The lower ionization potential of the cation terminated (111) or (0001) surfaces is related to a smaller surface dipole. The different ionization potentials can also affect the band alignment at weakly interacting interfaces [93].

According to these observations, the low ionization potential of the undoped ZnO films deposited at room temperature in pure Ar corresponds to a predominant Zn-terminated (0001) surface orientation. The surface orientation agrees with a preferred (0001) orientation observed in X-ray diffraction for identically prepared films (see Fig. 4.14[6]). A pronounced c-axis texture is almost exclusively observed for sputtered ZnO films (see e.g., [39, 94, 95] and other chapters of this book). With increasing oxygen content, the increase of ionization potential indicates a change of surface orientation, which agrees with a reduced texture in XRD (see Fig. 4.14). No significant change of ionization potential is observed for a substrate temperature of 200–300°C (see lower right graph of Fig. 4.13). Apparently, Zn-terminated (0001) surfaces are the predominant surface termination under these deposition conditions, in agreement with a pronounced (0001) texture in XRD (Fig. 4.14).

The Al-doped films deposited at room temperature show an ionization potential of 7.0–7.1 eV, independent on oxygen concentration. Reliable work function measurements of ZnO:Al films deposited with more than 10 % oxygen in the sputter gas were not possible due charging effects during measurement. Apparently, the presence of Al in the films stabilizes the (0001):Zn surface termination. ZnO:Al films deposited with 10 % oxygen in the sputter gas also exhibited a pronounced (0001) texture [70]. In contrast, an increase of substrate temperature leads to a reduced texture and an associated increase of ionization potential. This change is most likely related to the increase of the Al-content in the films with increasing substrate temperature (see Fig. 4.7). A higher Al content hence leads to a deviation from the pronounced (0001) texture, as also reported by Sieber et al. [96].

4.2.3.3 Core-Level Binding Energies

Because of the variation of the Fermi level position with respect to the band edges (see Fig. 4.12), the binding energies of the core levels will also change. Hence, the core level binding energies of semiconductors are not a good reference. However, the binding energy difference between the core levels and the

[6] The diffraction patterns in Fig. 4.14 were recorded in gracing incidence and plotted on a logarithmic scale and, therefore, have a different appearance compared with data taken in standard Bragg–Brentano (Θ–2Θ) mode and data plotted on a linear scale.

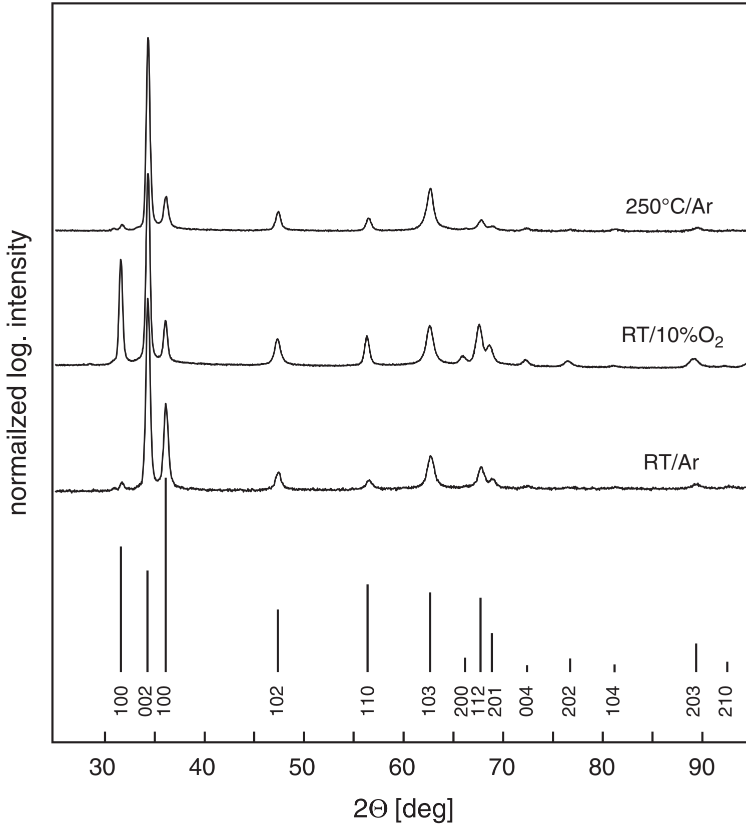

Fig. 4.14. Gracing incidence ($\Phi_0 = 2.2°$) X-ray diffraction patterns of undoped ZnO films deposited with identical parameters as those of films used for photoemission experiments. Intensities are plotted on a logarithmic scale to emphasize the low intensity features. The patterns were recorded using Cu Kα radiation ($\lambda = 1.54060$ Å). The thickness of the films is ~1 µm

valence band maximum $\mathrm{BE_{VB}(CL)}$ should be constant for a given material as they reflect the density of states. These values are essential for the determination of the band alignment at semiconductor interfaces [8,33]. Corresponding values for the Zn $2p_{3/2}$ and the O 1s core levels of sputter-deposited ZnO films in dependence on deposition conditions are given in Fig. 4.15. It is evident that the values depend on deposition conditions and on the doping of the films. An almost identical variation is observed for undoped (Zn,Mg)O films [59].

The variation in $\mathrm{BE_{VB}(CL)}$ and in the binding energy difference between the two core levels is explained by a superposition of two different effects. To begin with, undoped ZnO films show the highest $\mathrm{BE_{VB}(CL)}$ when the films are deposited at room temperature with pure Argon as sputter gas. The

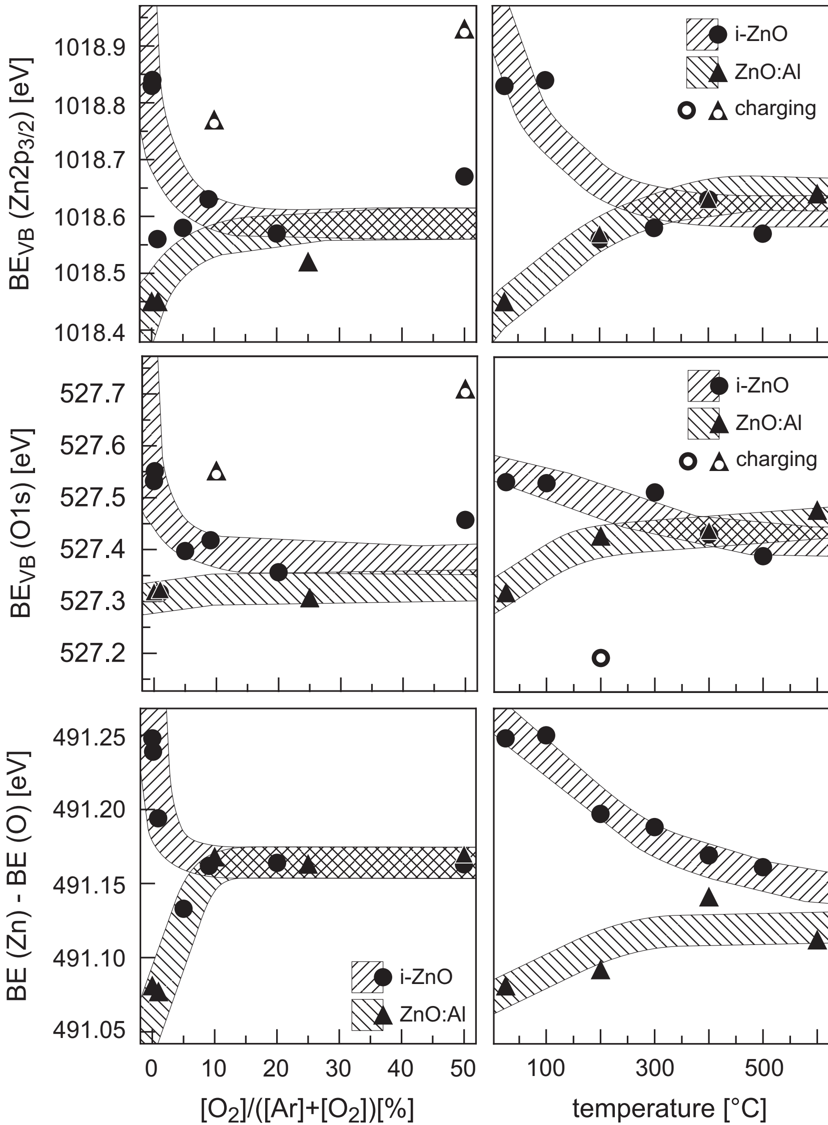

Fig. 4.15. Binding energy difference between Zn $2p_{3/2}$ and O 1s core levels and between the core levels and the valence band maximum. Films are deposited by dc magnetron sputtering from undoped and 2 % Al-doped ceramic targets at room temperature in dependence of sputter gas composition (*left*) and in pure Ar in dependence on substrate temperature (*right*). All films were deposited using a total pressure of 0.5 Pa, a sputter power density of 0.74 W cm^{-2} and a substrate to target distance of 10 cm

addition of oxygen to the sputter gas or the deposition at elevated substrate temperatures leads to the same values for $\mathrm{BE_{VB}(CL)}$, independent on the target material (undoped or doped). It is reasonable to assume that the values obtained under such conditions

$$\begin{aligned} \mathrm{BE_{VB}(O\,1s)} &= 527.4 \pm 0.1\,\mathrm{eV} \\ \mathrm{BE_{VB}(Zn\,2p_{3/2})} &= 1018.55 \pm 0.1\,\mathrm{eV} \\ \mathrm{BE(Zn\,2p_{3/2})} - BE(\mathrm{O\,1s}) &= 491.15 \pm 0.1\,\mathrm{eV} \end{aligned}$$

are representative for well-ordered crystalline ZnO. In contrast, films deposited at room temperature without addition of oxygen have to be expected to contain a considerable number of structural defects as the formation of well-ordered crystalline ZnO may be kinetically prohibited. Structural disorder can lead to a modification of the density of states in the valence band, which is well known for the extreme disorder in amorphous semiconductors (Urbach tails). However, X-ray diffraction patterns (see Fig. 4.14) of films prepared in the same way as those used for the data in Fig. 4.15 show clearly the long range order of the wurtzite lattice and provide no evidence for an amorphous structure of the ZnO films. Nevertheless, local disorder can be present as a high density of crystallographic point defects or a high density of stacking faults [96,97]. These do not affect the long range order but modify the local chemical bonding and thereby influence the electron wave functions and the local charge distribution.

Local disorder might affect the valence band maximum energy of ZnO also via a modification of orbital hybridization. The Zn 3d levels are low lying d-states, which hybridize with the O 2p states and thus contribute to the valence band density of states [98–100]. Any change in local symmetry will also affect the hybridization between the Zn 3d and O 2p states. It is expected that the p–d hybridization leads to a lowering of the valence band maximum in ZnO (see discussion of band alignment between II–VI compounds in Sect. 4.3.1). A reduction of the p–d interaction by disorder would thus lead to an upward shift of the valence band maximum and consequently to an increase of $\mathrm{BE_{VB}(CL)}$ as indeed observed in the experiments.

Instead of modifying the density of states, local disorder might also lead to a poorer screening of the core hole as a result of reduced polarizability of the lattice. This might also account for the larger $\mathrm{BE_{VB}(CL)}$ values of films deposited at room temperature in pure Ar.

The variation of band alignment on the deposition conditions suggests a modification of the density of states as origin for the changes in $\mathrm{BE_{VB}(CL)}$ (see Sect. 4.3.3). However, a detailed comparison of valence band spectra provides no hint for such an explanation as no changes in the shape and width of the spectra are observed (see Fig. 4.16). There are also no evident changes in the distance between Zn 3d level and the valence band maxima in these spectra. Hence, although the variation in $\mathrm{BE_{VB}(CL)}$ for undoped ZnO suggests the presence of a strong local disorder for films deposited at room

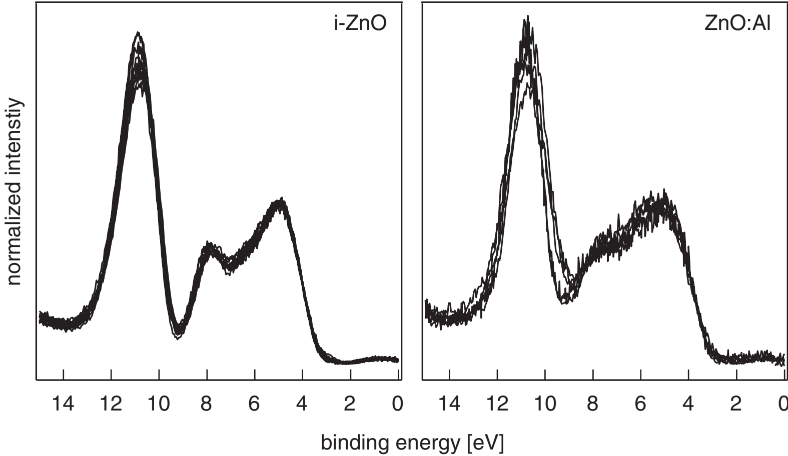

Fig. 4.16. Comparison of He II ($h\nu = 48.86\,\text{eV}$) valence band spectra of sputter deposited undoped (*left*) and Al-doped (*right*) ZnO films. Different *curves* belong to different sputter conditions as substrate temperature and oxygen partial pressure. The binding energies of the spectra were shifted for better comparison of shapes of the spectra

temperature in pure Ar, a detailed description of the influence of the disorder cannot be given yet.

In addition to the local disorder, the high free-electron concentration of the Al-doped films deposited at low substrate temperature and with less than $\sim$2 % oxygen in the sputter gas also contributes to the variation in BE_{VB}(CL). The free electrons lead to an increased screening of the positive charge of the core hole, which is created by the photoemission process. The additional screening reduces the apparent binding energy of the core hole. The effect has been systematically observed for Sb-doped SnO_2 [55, 56] and also for ITO [57, 58]. The screening of the core hole affects not only the apparent binding energy of the core level and thereby BE_{VB}(CL), but also the line shape of the core levels due to the occurrence of plasmon satellites, which has already been mentioned earlier. The processes and their influence on line shape are illustrated in Fig. 4.17.

According to Fig. 4.15, a $\text{BE}_{\text{VB}}(\text{Zn}\,2\text{p}_{3/2})$ of highly doped films is $\sim$150 meV smaller than those of films deposited at higher substrate temperatures or with addition of oxygen to the sputter gas. For ITO, the difference in $\text{BE}_{\text{VB}}(\text{In}\,3\text{d}_{5/2})$ between highly doped and undoped material amounts to $\sim$500 meV, which is considerably larger than for ZnO. Most likely, the reduction of the apparent core-level binding energy in ZnO by screening is superimposed by an increase in binding energy, which is observed for identically prepared undoped ZnO films. The difference in $\text{BE}_{\text{VB}}(\text{Zn}\,2\text{p}_{3/2})$ for i-ZnO and ZnO:Al for films prepared at room temperature with pure Ar as sputter gas amounts to $\sim$400 meV, which is comparable to the shift observed for ITO.

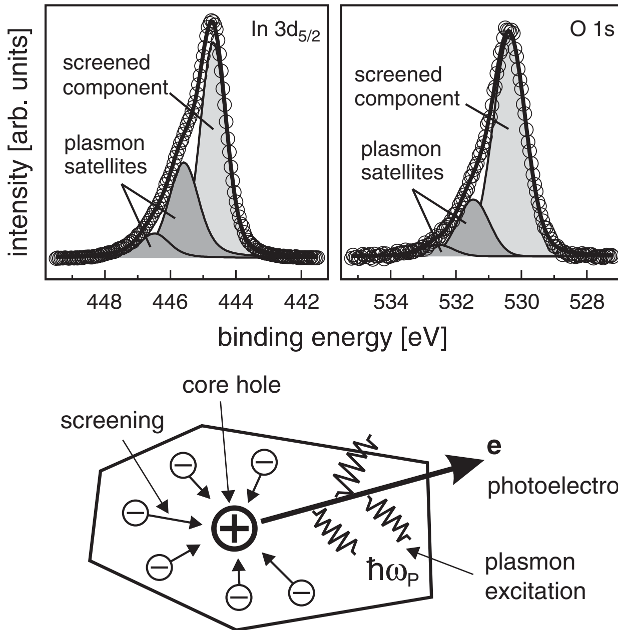

Fig. 4.17. Photoelectron line shape of the In $3d_{5/2}$ and O 1s core levels of a highly doped ITO film [58]. The high concentration of free electrons leads to excitation of plasmons, which give rise to shoulders at the high binding energy side of the main emission. Furthermore, the polarization of the free electron gas leads to an additional screening of the core hole, which reduces the binding energy of the main emission component. The plasmon energy depends on the electron concentration and amounts to 0.5–1 eV for the highest doped films [56, 101]

4.3 The CdS/ZnO Interface

4.3.1 Band Alignment of II–VI Semiconductors

The CdS/ZnO interface is of particular importance in Cu(In,Ga)Se_2 thin film solar cells because it is used in the standard cell configuration (Fig. 4.2). A first experimental determination of the band alignment at the ZnO/CdS interface has been performed by Ruckh et al. [102]. The authors have used ex-situ sputter-deposited ZnO films as substrates. The interface formation was investigated by stepwise evaporation of the CdS compound from an effusion cell. Photoelectron spectroscopy revealed a valence band offset of $\Delta E_{\mathrm{VB}} = 1.2\,\mathrm{eV}$. An identical value of 1.18 eV has been derived using first-principles calculations [103]. With the bulk band gaps of CdS and ZnO of 2.4 and 3.3 eV, respectively, this leads to a conduction band offset 0.3 eV, with the conduction band minimum of CdS being above the one of ZnO. This value is frequently used in the literature for modeling of the Cu(In,Ga)Se_2 thin film solar cells [14, 104, 105].

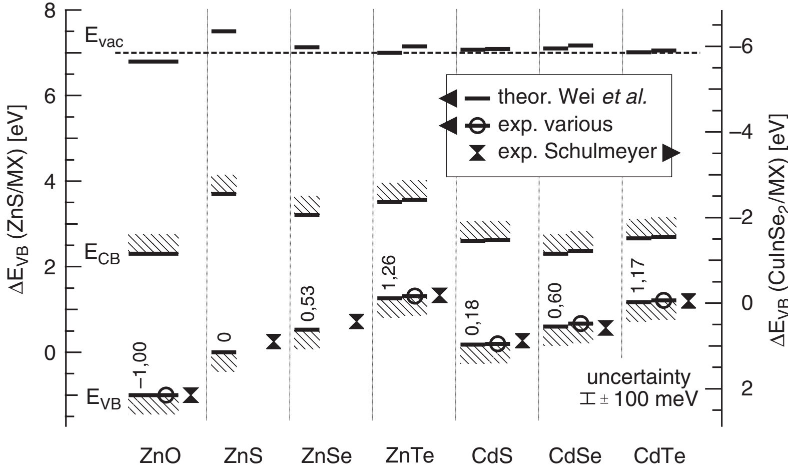

Fig. 4.18. Band alignment of II–VI compound heterointerfaces calculated ab-initio by density functional theory [103] (*left section* of each column). The valence band maxima are given with respect to the valence band maximum of ZnS as in the original publication by Wei et al. Available experimental values for the band alignments of individual interfaces are shown in the *middle section* of each column. Corresponding experimental details and references are given in Table 4.1. The *right section* contains valence band offsets ΔE_{VB} of Cu(In,Ga)Se_2/II–VI heterointerfaces as determined by Schulmeyer et al. [36, 106, 107] (*right axis*). The energy difference between the *left* and *right axes* corresponds to the valence band offset at the $CuInSe_2$/ZnS interface. Vacuum levels as determined for the different materials are shown at the *top*. Except for ZnS the vacuum energies are at approximately the same energy, indicating that only small interface dipoles occur

The calculated band alignments of the II–VI semiconductors including ZnO [103] are shown in Fig. 4.18. The energies of the valence band maxima are referenced to the valence band maximum of ZnS. Included in the figure is a selection of experimental results for band alignment at different in situ prepared II–VI semiconductor interfaces (for detailed values and references see Table 4.1). All experimental results agree with the theoretical prediction within 100 meV. An additional justification of the theoretical band alignments is given by the valence band offsets between the II–VI compounds and Cu(In,Ga)Se_2. These interfaces are prepared by evaporation of II–VI compounds onto oxide-free device-grade Cu(In,Ga)Se_2 surfaces [36,106,107]. Such surfaces can be made available using the decapping procedure by heating-off of a Se cap layer, which is deposited onto a freshly prepared Cu(In,Ga)Se_2 layer without breaking vacuum. The procedure allows for storage and transport of the samples in air.

The agreement between the calculations and the various experimental results is excellent. This indicates the wide applicability of the calculated band alignments. The general behavior also confirms the original value given

Table 4.1. Valence band offsets at interfaces of II–VI compounds determined by photoelectron spectroscopy

Interface	ΔE_{VB} (eV)	Ref.	Growth	Crystallinity	Lattice
ZnO/CdS	1.2	[102]	MBE	Poly	Mismatched
ZnO/ZnTe	2.37	[108]	Sputtering	Poly	Mismatched
CdTe/ZnTe	0.1	[108]	Sputtering	Poly	Mismatched
CdS/CdTe	1.01	[109]	MBE	Poly	Mismatched
CdTe/ZnTe	0.1	[110]	MBE	Single	Mismatched
CdSe/ZnTe	0.64	[111]	MBE	Single	Matched

by Ruckh et al. [102] for the band alignment at the ZnO/CdS interface and its use in device simulation. It also provides a valuable tool for the selection of different buffer layers in solar cells. In general, Zn-containing compounds as ZnS, ZnSe, and ZnTe result in a considerably larger conduction band offset to ZnO compared with Cd-containing compounds as CdS, CdSe, and CdTe. This is related to the larger band gaps of the Zn- compared to the Cd-chalcogenides in combination with the similar valence band maximum energies for the same anions.

Although the band alignment at the interfaces seems to be well established from the data presented in Fig. 4.18 and Table 4.1, the influence of the sputter deposition on the electronic properties of the interface has not yet been addressed systematically. Such studies are required to identify the fundamental parameters that govern interface chemistry and electronic properties. In the following we describe our recent results on the CdS/ZnO interfaces. Although being rather extensive, so far only CdS films prepared by thermal evaporation have been used. In high efficiency solar cells, the CdS films are prepared by chemical bath deposition [15], which might lead to different interface properties. However, noticeable efficiencies can also be achieved using evaporated CdS films [112]. Furthermore, Weinhardt et al. have studied the band alignment at the CdS/ZnO interface by sputter depth profiling of a layer structure used for solar cells, i.e., a chemical bath deposited CdS buffer layer and sputter-deposited undoped ZnO [113]. Valence and conduction band offsets are determined as $\Delta E_{VB} = 0.96 \pm 0.15\,\text{eV}$ and $\Delta E_{CB} = 0.1 \pm 0.15\,\text{eV}$. The valence band offset lies well within the range of values presented in the following and therefore suggests that the electronic interface properties are only little affected by the CdS deposition technique.

4.3.2 Sputter Deposition of ZnO onto CdS

A determination of the band alignment at the CdS/ZnO interface where ZnO has been stepwise deposited by magnetron sputtering has been published by Venkata Rao et al. [71]. A more extended series of spectra recorded during ZnO deposition by dc magnetron sputtering onto CdS are presented in Fig. 4.19. During ZnO deposition the sample was held at room temperature.

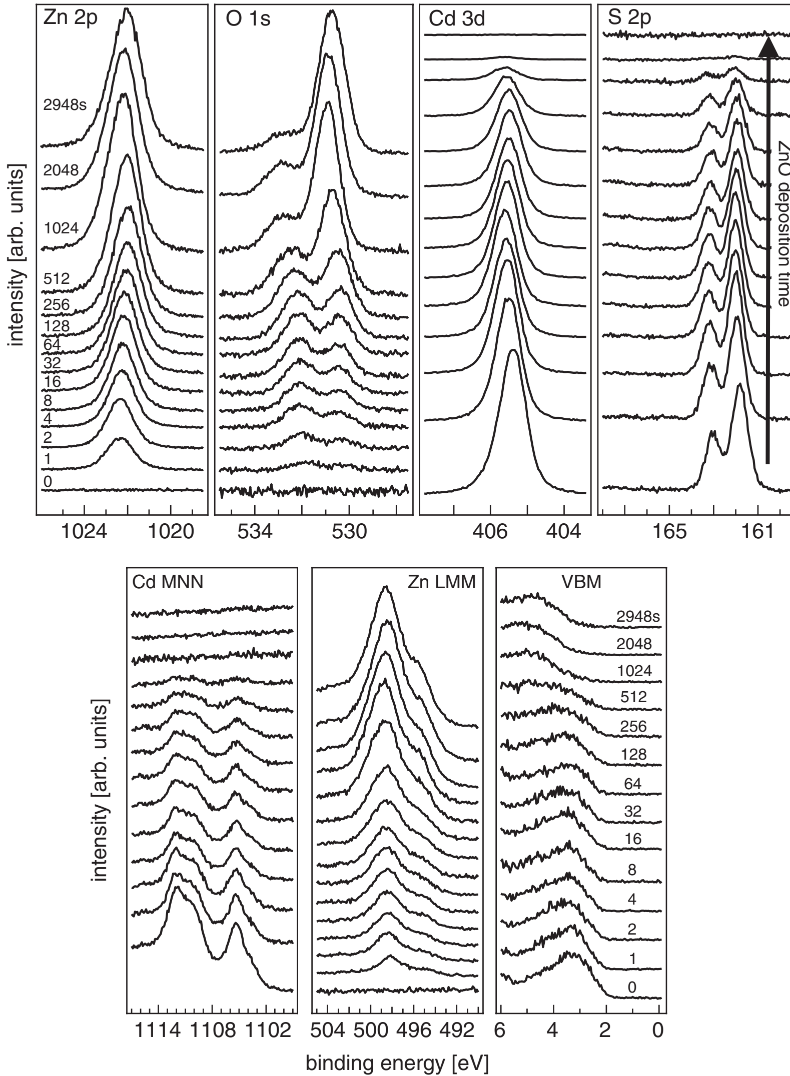

Fig. 4.19. Core levels (Zn $2p_{3/2}$, O 1s, Cd $3d_{5/2}$, S 2p), Auger levels (Cd MNN, Zn LMM) and valence bands (VB) recorded during stepwise sputter deposition of ZnO onto a CdS substrate. The deposition times are indicated in seconds. All spectra were excited using monochromatic Al Kα radiation ($h\nu = 1486.6$ eV). ZnO was deposited from an undoped target using pure Ar as sputter gas and a sputter power of 5 W (dc)

The bottom spectra are taken from a freshly evaporated CdS film. The only emissions observed are from Cd and S core levels and Auger levels and from the valence band region. With increasing deposition time of ZnO, the Cd and S levels are attenuated, while the emissions from the growing ZnO film

are increasing. The valence band spectra of CdS are gradually replaced by those of ZnO, which is evident from the higher binding energy position of the valence band maximum. It is recalled that the escape depth of the photoelectrons is ~1–2 nm. The low attenuation of the substrate emissions after the first deposition step corresponds to a nominal ZnO film thickness of less than 1 Å.[7] To achieve such a low deposition rate by dc magnetron sputtering, a low sputter power of 5 W (2 in.-target) has been used.

4.3.2.1 Interface Chemistry and Film Growth

A chemical reaction at the interface can, in principle, result in additional components of the core levels or Auger lines, or in a different energy shift of the different lines of the substrate or film. In particular, an oxidation of the CdS substrate should result either in the occurrence of SO_x emissions at binding energies of 166–169 eV [114], or in the change of the line shape of the Cd MNN Auger emission.[8] No such effects are observed. In addition, the substrate emission lines (Cd 3d, O 1s, Cd MNN) show only very small and nearly parallel binding energy shifts (see also Fig. 4.20). An oxidation of the substrate can, therefore, be excluded within the sensitivity of the experiment. Hence, even for sputter-deposited oxide films, oxidation of the substrate is not inevitable. This might be explained by the fact that most of the oxygen involved in the growth process is present as stable O_2 molecules.

In contrast to the substrate emissions, the line shape of the growing O 1s emission changes significantly with film thickness. The spectra are the same as those shown in Fig. 4.9a. For low coverage, the high binding energy component dominates. The behavior has been explained in Sect. 4.2.2.2 by the formation of peroxide species due to the inability of the CdS surface to dissociate the adsorbed O_2 molecules. This also explains why no oxidation of the substrate is observed during growth. It has been argued in Sect. 4.2.2.2 that dissociation of O_2 is facilitated on In_2S_3 and $Cu(In,Ga)Se_2$ surfaces, since no peroxide is observed on these surfaces at low ZnO coverage (see Fig. 4.9b,d). In fact, during deposition of ZnO onto In_2O_3 and $Cu(In,Ga)Se_2$, oxidation of the substrate is observed by XPS (see Sects. 4.5 and 4.4), which supports the interpretation given in Fig. 4.10.

At low coverage, the binding energy of the ZnO O 1s level (low binding energy O 1s component) does not shift in parallel to the binding energy of the Zn $2p_{3/2}$ level. The binding energy difference $\mathrm{BE}(\mathrm{Zn}\,2p_{3/2}) - \mathrm{BE}(\mathrm{O}\,1s)$ is up to 0.7 ± 0.1 eV larger than the value observed for the thick ZnO film. This is evident from the splitting of the two curves for ZnO at low deposition times in Fig. 4.20. An identical behavior is observed in all experiments where ZnO has been deposited onto CdS, In_2S_3, and $Cu(In,Ga)Se_2$ (see Sects. 4.4 and 4.5,

[7] The deposition rate is ~5 nm min^{-1}.

[8] Chemical shifts are not very pronounced for the Cd 3d core level [114] and might therefore be hardly identified.

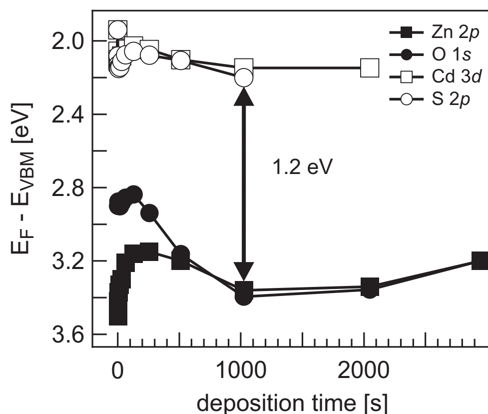

Fig. 4.20. Evolution of the CdS and ZnO valence band maxima as derived from the binding energies of the core levels by subtracting $BE_{VB}(CL)$ values determined from the CdS substrate and the thick ZnO film, respectively [71]. The different evolution of the Zn 3d and O 1s binding energies is attributed to an amorphous structure of the ZnO layer during the initial growth. The thickness of the amorphous layer is ∼2 nm. The ZnO films were deposited by magnetron sputtering from an undoped ZnO target at room temperature using 5 W dc power

Figs. 4.30 and 4.37, and [70]) and also during deposition of (Zn,Mg)O onto CdS [71]. Therefore, the different evolution of the oxygen and zinc core-level binding energies can not be related to the observation of the peroxide surface species, as no such species is observed during initial growth on In_2S_3 and $Cu(In,Ga)Se_2$ (see Fig. 4.9).

For the reverse deposition sequence (CdS on ZnO), the binding energy difference between the Zn 2p and O 1s core levels remains constant during deposition [70, 90]. However, in these experiments the binding energy difference between the Cd 3d and S 2p core levels is different at low coverage [70,90]. An identical behavior is observed during growth of CdS onto SnO_2 [115] and during growth of CdTe onto In_2O_3 [116]. It is, therefore, clear that the different binding energy difference between anion and cation core levels at low coverage cannot be due to a chemical interaction at the interface but is rather related to the structure of the growing film.

Yoshino et al. [117] have studied the growth of magnetron-sputtered ZnO films on different substrates using transmission electron microscopy and X-ray diffraction. A crystalline nucleation layer of ZnO is only observed on surfaces of crystalline materials such as sapphire and Au. In the case of unordered surfaces like glass or Al, which are either amorphous or develop an amorphous oxide layer during deposition, the ZnO nucleation layer is highly disordered or amorphous. Similar results were observed by Mirica et al. [97] who compared the growth of ZnO on oxide forming (Si) and nonoxide forming (Pt)

substrates. Sieber et al. [96] also found a highly disordered layer at the Si/ZnO interface consisting of an amorphous SiO_2 and an nanocrystalline ZnO layer.

The formation of an amorphous nucleation layer of ZnO on (poly-) crystalline chalcogenides as CdS, In_2S_3 and $Cu(In,Ga)Se_2$ could be related to the interface chemistry. In the case of CdS, oxygen dissociation and therefore formation of a crystalline layer is hindered. For In_2S_3 and $Cu(In,Ga)Se_2$ (see following sections), oxygen dissociation at the surface leads to a partial oxidation of the substrate surface, which also destroys the regular atomic arrangement at the surface.

Following these studies, a microstructure of sputter-deposited ZnO films on polycrystalline CdS substrates is outlined in Fig. 4.21. The different evolution of the Zn 2p and O 1s binding energies can consequently be attributed to the amorphous ZnO nucleation layer with a different chemical bonding between Zn and O. The model is also valid for polycrystalline In_2S_3 and $Cu(In,Ga)Se_2$ substrates and for deposition of (Zn,Mg)O films, as these show the same behavior (see Figs. 4.20 and 4.24). It is not clear whether an amorphous nucleation layer occurs also when the ZnO is deposited by other techniques as MBE, CVD, or PLD, as no data are available for such interfaces. In addition, the influence of the polycrystallinity of the substrates is not clear so far.

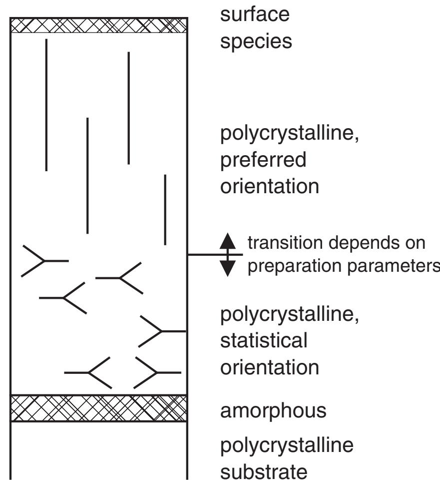

Fig. 4.21. Microstructure of ZnO films on polycrystalline CdS substrates following models for amorphous substrates suggested in literature [96, 97, 117]. No chemical reaction between CdS and ZnO is identified suggesting a sharp interface. The initial growth of ZnO proceeds with a highly disordered or amorphous structure, giving rise to the different evolution of the Zn 2p and O 1s core-level binding energies at low coverage, which is generally observed at low coverage during sputter deposition of ZnO onto CdS (see Figs. 4.20 and 4.24 and [71]) The thickness of the amorphous layer is $\sim$2 nm

4.3.2.2 Band Alignment at the Interface

The valence band offset at the interface can be directly evaluated from the data in Fig. 4.20. For deposition times between 500 and 2 000 s, the difference in valence band maxima positions for CdS and ZnO is almost constant with an average value of $\Delta E_{\mathrm{VB}} = 1.2 \pm 0.1\,\mathrm{eV}$. This is in excellent agreement with the value from Ruckh et al. [102] for the ZnO/CdS interface and with the theoretical calculation by Wei et al. [103], suggesting that there is only little influence of the preparation conditions on the band alignment. However, given the highly asymmetric microstructure of the CdS/ZnO and the ZnO/CdS interfaces, which is expressed by Fig. 4.21, the agreement between the valence band offsets for the two orientations cannot necessarily be expected. In addition the agreement turns out to be fortuitous when data for additional interfaces are taken into account (see Sect. 4.3.3).

The energy band diagram of the interface as determined from the spectra is shown in Fig. 4.22. The positions of the vacuum energy, which is determined from UPS measurements of the CdS substrate and the thick ZnO layer are included. Taking these values, there appears to be a large discontinuity in the vacuum energy (dipole potential) at the interface, which could be attributed to a charge transfer at the interface. The large discontinuity in the vacuum level is a result of the low electron affinity of the ZnO, which is due to the (0001):Zn surface termination obtained under the selected preparation conditions of the ZnO film (see Sect. 4.2.3.2). However, when the details of the microstructure (Fig. 4.21) are taken into account, the ZnO layer close to the interface is not *c*-axis but rather randomly oriented. Therefore, a larger electron affinity has to be used, which consequently leads to a smaller interface dipole potential as illustrated in the right part of Fig. 4.22. A similar model, although with a reversed order of electron affinities has been used by Löher et al. to describe the band alignment between II–VI compounds and layered transition metal dichalcogenides [93].

4.3.3 Dependence on Preparation Condition

To study the influence of the preparation conditions on the interface properties, a number of different interfaces have been prepared. Details of the preparation and the determined valence band offsets are listed in Table 4.2. The experiments include not only both deposition sequences, but also interfaces of Al-doped ZnO films, which have been conducted to elucidate the role of the undoped ZnO film as part of the $\mathrm{Cu(In,Ga)Se_2}$ solar cell. Details of the experimental procedures and a full set of spectra for all experiments are given in [70]. Table 4.2 includes a number of interfaces between substrates of undoped ZnO films and evaporated CdS layers (ZOCS A-D). In a recent publication [90] different values were given for the valence band offsets, as the dependence of $\mathrm{BE_{VB}(CL)}$ on the deposition conditions was not taken into account in this publication.

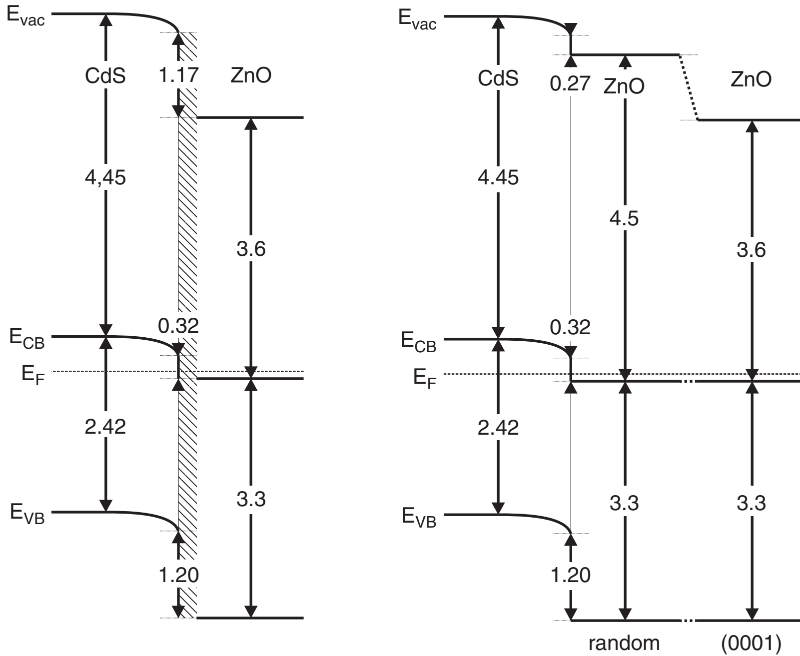

Fig. 4.22. Energy band diagram at the CdS/ZnO interface. All values are given in electronvolt. The *left side* shows the diagram where the vacuum energy of the ZnO layer is determined from the thick ZnO film. For the selected preparation conditions (room temperature, 100 % Ar) the film is (0001) textured with a Zn termination (see Sect. 4.2.3.2), which results in a large discontinuity of the vacuum energy at the interface. According to the microstructure of the interface (Fig. 4.21), the ZnO close to the CdS is not oriented leading to a larger electron affinity of ~4.5 eV and hence to a lower discontinuity in the vacuum energy. In the left part of the figure, the amorphous ZnO nucleation layer is indicated by the *shaded area*. The amorphous region is omitted in the right part for clarity

The experimentally determined valence band offsets span quite a large range from $\Delta E_{\mathrm{VB}} = 0.84 - 1.63\,\mathrm{eV}$. The variation of 0.8 eV is considerably larger than the experimental uncertainty, which is $\pm 0.1\,\mathrm{eV}$ for most experiments with only a few exceptions. Experiments with a larger uncertainty have been omitted.

The experimental procedure for the determination of the valence band offsets directly relies on the core level to valence band maximum binding energy differences $\mathrm{BE_{VB}(CL)}$ as described in Sect. 4.1.3 and Fig. 4.3. The corresponding values for the Zn $2p_{3/2}$ and the Cd $3d_{5/2}$ core level are therefore included in Table 4.2. These values are determined directly from the respective interface experiments. With two exceptions (CSZA-E and ZACS-C), the values for the Zn $2p_{3/2}$ core level show the same dependence on deposition conditions as given in Fig. 4.15. For these two exceptions, also the Fermi level position

Table 4.2. Details of experiments on different CdS/ZnO interfaces studied by photoelectron spectroscopy[a]

Label	Interface	ZnO	CdS (°C)	ΔE_{VB} (eV)	Zn-VB (eV)	Cd-VB (eV)
CSZO-A	CdS/ZnO	5 W	250	1.20	1018.85	403.46
ZOCS-A	ZnO/CdS	3 W	25	0.84	1018.89	403.41
ZOCS-C	ZnO/CdS	450°C	25	1.00	1018.74	403.45
ZOCS-D	ZnO/CdS	10 % O_2	25	1.11	1018.54	403.48
Ref. [102]	ZnO/CdS	RF	25	1.10	1019.1	403.4
CSZA-A	CdS/ZnO:Al	S	25	1.63	1018.44	403.48
CSZA-B	CdS/ZnO:Al	10 % O_2	250	1.17	1018.53	403.58
CSZA-D	CdS/ZnO:Al	S	250	1.57	1018.44	403.53
ZACS-A	ZnO:Al/CdS	S	25	1.43	1018.45	403.42
ZACS-D	ZnO:Al/CdS	10 % O_2	25	1.37	1018.55	403.52

[a]Unless indicated, ZnO films were sputter deposited using the standard parameters "S," which are defined as $T = 25°\text{C}$, $p = 0.5\,\text{Pa}$ (100 % Ar), $P = 15\,\text{W}$ (dc). All CdS films were prepared by thermal evaporation from the compound. Uncertainties of valence band offsets ΔE_{VB} and core level to valence band maximum binding energy differences $BE_{VB}(CL)$ ("Zn-VB" for ZnO and "Cd-VB" for CdS) are typically ± 0.1 eV. Experiments with larger uncertainties have been omitted. The ZnO:Al films were deposited from targets with an Al content of 2 wt %. Details of the experimental procedures and a full set of spectra for all experiments are provided in [70]. The valence band offsets given for the interfaces ZOCS-A to ZOCS-D differ from those in a recent publication [90] in which a constant value of $BE_{VB}(CL)$ for Zn 2p and O 1s levels have been used. Data from Ruckh et al. [102] are also included. For a better comparison we have adopted their value determined from the core-level binding energy difference (1.1 eV) instead of the value determined directly from the valence band spectra (1.2 eV)

is much lower than expected (BE(VB) ≈ 3.2 eV instead of ~ 3.6 eV). As the ZnO:Al films are deposited at 450°C substrate temperature in these experiments, the deviating film properties might be related to diffusion of species from the substrates. The $BE_{VB}(CL)$ for the Cd $3d_{5/2}$ level of the CdS films are 403.46 ± 0.05, which is in good agreement with literature [36, 102, 115]. All CdS films were deposited by thermal evaporation from the compound. No significant dependence of the film properties with substrate or source temperature has been noticed so far.

To account for a possible influence, the experimental valence band offsets are plotted vs. $BE_{VB}(\text{Zn } 2p_{3/2})$ in Fig. 4.23. For comparison, values obtained for interfaces between thermally evaporated CdS films and undoped (Zn,Mg)O films prepared by rf magnetron sputtering have been included [59]. The agreement between the valence band offsets of ZnO (squares) and (Zn,Mg)O (triangles) is due to the fact that the larger band gap of (Zn,Mg)O is due to a higher conduction band minimum and a nearly zero valence band offset between these two materials [71,118]. According to Fig. 4.23, the experimental valence band offsets can be divided into different groups, which are indicated by circled numbers.

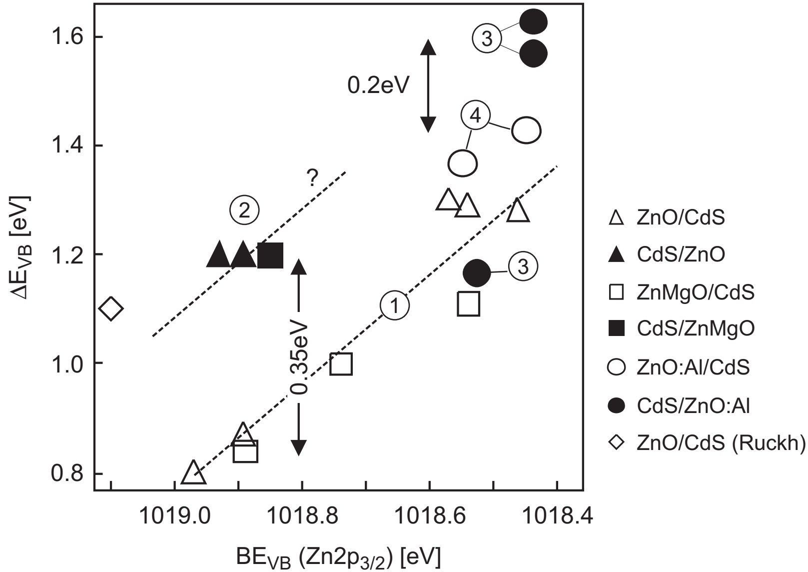

Fig. 4.23. Valence band offsets for CdS/ZnO, CdS/(Zn,Mg)O and CdS/ZnO:Al interfaces as determined by photoemission experiments. *Solid* symbols are for sputter deposition of the oxides onto CdS, *open* symbols are for deposition of CdS onto the oxides. The value from Ruckh et al. [102] is included (*diamonds*). The *circled numbers* serve to classify the different values as described in the text

1. The valence band offsets for the interfaces where CdS was evaporated onto undoped ZnO (open squares) or (Zn,Mg)O (open triangles) show a linear dependence on $BE_{VB}(Zn\,2p_{3/2})$. Using ordered ZnO films as substrates ($BE_{VB}(Zn\,2p_{3/2}) \sim 1018.5$ eV; see Sect. 4.2.3.3) results in a valence band offset of $\Delta E_{VB} = 1.2 \pm 0.1$ eV, which agrees with the theoretical value of Wei and Zunger [103]. The larger values of $BE_{VB}(Zn\,2p_{3/2})$ correspond to ZnO layers deposited at room temperature in pure Ar, which show a high local disorder. Using such films as substrates for CdS deposition results in a valence band offset of $\Delta E_{VB} = 0.85 \pm 0.1$ eV. The disorder, therefore, shifts the valence band maximum of ZnO upwards in energy. This leads both to a smaller valence band offset and to a larger binding energy of the core levels with respect to the valence band maximum $BE_{VB}(Zn\,2p_{3/2})$. The valence band offset determined for a ZnO film prepared with standard deposition conditions (room temperature, 100 %Ar) is smaller than the one obtained when the ZnO film is deposited with the addition of oxygen to the sputter gas. An influence of the ionization potential of the ZnO surface on the band alignment might therefore also be considered as origin for the variation in band alignment. The ionization potential of the ZnO film deposited with oxygen is ~0.8 eV larger for standard deposition conditions (see Sect. 4.2.3.2). However, a higher substrate temperature does

not lead to a larger ionization potential (see Fig. 4.2.3.2) but also results in a larger valence band offset. It is, therefore, not likely that the different ionization potential is the origin for the variation in band alignment. This agrees with theoretical considerations [119], which indicate that a variation of band alignment with surface orientation is only possible for interfaces between nonisovalent semiconductors and, therefore, not for the interface between the two II–VI semiconductors ZnO and CdS.
The experimental result of Ruckh et al. [102], which is obtained for comparable preparation conditions, deviates from the general behavior observed in our own data. The reason for this deviation is not clear.

2. The interfaces prepared by sputter deposition of ZnO (filled square) or (Zn,Mg)O (filled triangles) exhibit a valence band offset of $\Delta E_{\mathrm{VB}} = 1.2\,\mathrm{eV}$. The ZnO and (Zn,Mg)O films were prepared at room temperature in pure Ar and therefore exhibit a large disorder and a large $\mathrm{BE_{VB}}(\mathrm{Zn\,2p_{3/2}})$. Compared with the interface with reverse deposition sequence, the offset is ~0.35 eV larger. This indicates a rather strong influence of the deposition sequence on the band alignment at the CdS/ZnO interface, which is most likely related to the amorphous nucleation layer when ZnO is deposited onto CdS.
   Unfortunately, there are currently no band alignments for the CdS/ZnO interface available, where undoped ZnO is deposited using other deposition parameters or deposition techniques. Such data would be important to distinguish between different influences on the band alignment. The use of higher substrate temperatures or oxygen in the sputter gas during ZnO deposition should lead to ordered ZnO films with a smaller $\mathrm{BE_{VB}}(\mathrm{Zn\,2p_{3/2}})$. It would be interesting to know if the resulting band alignment shows the same dependence as for the reverse deposition sequence. In this case the valence band offsets should follow the upper dashed line in Fig. 4.23 ("?") and a ΔE_{VB} of ~1.6 eV should result.
3. The valence band offsets for deposition of ZnO:Al on CdS are ~1.6 eV when the ZnO:Al films are prepared using pure Ar, which leads to degenerately doped material (CSZA-A and CSZA-D). Deposition of ZnO:Al films with a sputter gas containing 10 % O_2 results in a low doped material (see Sect. 4.2.3.1). For such deposition conditions (CSZA-B) a valence offset of ~1.2 eV is obtained.
   The difference of 0.4 eV is related to *Fermi level pinning* in the CdS substrate, which becomes evident by plotting the evolution of the valence band maxima in dependence on deposition time (left graph in Fig. 4.24). The Fermi level pinning is expressed by the observation that the valence band maximum binding energy in CdS lies always between $E_{\mathrm{F}} - E_{\mathrm{VB}} = 1.8 - 2.2\,\mathrm{eV}$. These limits hold for a large set of experiments performed in the surface science group in Darmstadt. They are observed without exception for any used CdS source temperatures (growth rate), substrate temperatures, and substrate materials as ZnO, SnO_2, CdTe, and $CuInSe_2$.

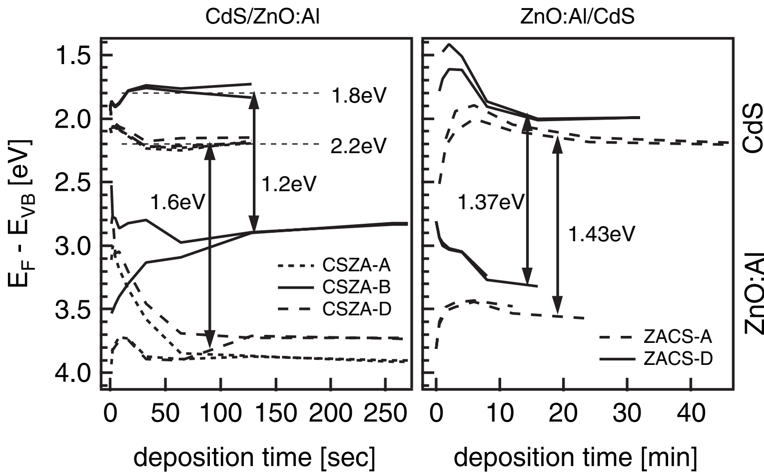

Fig. 4.24. Evolution of CdS and ZnO valence band maxima positions during sputter deposition of ZnO:Al onto CdS (*left*) and during evaporation of CdS onto ZnO:Al (*right*). The Fermi level in CdS is always within 1.8–2.2 eV above the valence band maximum (Fermi level pinning)

The Fermi level pinning is related to the defect structure of the material and therefore to the preparation of the CdS films.[9] The particular defects, which lead to the pinning of the Fermi level in CdS, are, however, not yet identified.

Since the position of the Fermi level in the CdS substrate is obviously restricted to 1.8–2.2 eV, the band alignment is determined by the Fermi level position in the ZnO:Al film at low coverage. This can also be extracted from Fig. 4.24. The Fermi level at very low coverage ($\leq$2 nm) cannot be determined unambigously because of the different evolution of the Zn 2p and O 1s binding energies, which has been attributed to the amorphous nucleation layer (see Sect. 4.3.2). A unique Fermi level position in the growing ZnO film can be determined only for deposition times $\geq$100–150 s, which correspond to a film thickness of $\sim$2 nm. The obtained values of $E_F - E_{VB} \approx 3.8$ eV for degenerately doped ZnO:Al deposited in pure Ar and of $E_F - E_{VB} \approx 3.0$ eV for undoped ZnO:Al deposited with 10 % oxygen are close to the values obtained for very thick films. Accordingly, there are almost no further changes of the Fermi level position for larger deposition times. This corresponds to a very fast establishing of the bulk Fermi level position in growing ZnO:Al films, which must be associated with a high defect concentration. It is suggested that this behaviour is related to the amorphous nucleation layer.

[9] All CdS films were evaporated from resistively heated Al_2O_3 crucibles using 99.999 % purity CdS source material.

The Fermi level pinning in CdS and the fast establishing of the Fermi level in ZnO:Al determine the band alignment at the interface: (1) The valence band offset determined for the CdS/ZnO:Al interfaces with degenerately doped ZnO films ($E_F - E_{VB} \geq 3.8\,eV$) cannot be lower than $3.8 - 2.2 = 1.6\,eV$. This is exactly the value derived from the corresponding experiments. (2) The valence band offset for ZnO:Al films deposited with addition of oxygen ($E_F - E_{VB} \leq 3.0\,eV$) cannot be larger than $3.0 - 1.8 = 1.2\,eV$, which is again the value determined in the experiment.

4. The experiments where ZnO:Al is used as substrate for the deposition of CdS give similar valence band offsets of $\Delta E_{VB} = 1.4 \pm 0.1\,eV$ for degenerately doped ZnO:Al and for films where oxygen has been added to the sputter gas. Apparently, Fermi level pinning does not contribute to the band alignment in this case. This is related to the large change of the Fermi level in the ZnO:Al substrates. The large difference of the Fermi level position of degenerately doped ZnO:Al ($E_F - E_{VB} = 3.8\,eV$) and of compensated ZnO:Al (2.8 eV) is strongly decreased during CdS deposition onto the substrates (see right part of Fig. 4.24). Hence the Fermi level is not pinned in the ZnO:Al substrates but can change considerably during interface formation. This supports that the fast establishing of the Fermi level position in growing ZnO:Al films described in point 3 is related to the amorphous nucleation layer.
   The valence band offsets determined for the ZnO:Al/CdS interfaces ($1.4 \pm 0.1\,eV$) are 0.2–0.4 eV larger than the values obtained for interfaces where undoped ZnO or (Zn,Mg)O films have been used as substrate. This points toward an influence of the Al content in the ZnO film on the band alignment. An explanation for this cannot be given yet.

4.3.4 Summary of CdS/ZnO Interface Properties

No interface reaction is observed at the CdS/ZnO interfaces. Even the sputter deposition of ZnO onto CdS with or without oxygen in the sputter gas does not lead to an increased reactivity. This is most likely related to the poor ability of the CdS and ZnO surfaces to dissociate oxygen atoms (compare Sect. 4.2.2.2 and discussion of the reactivity in Sects. 4.4 and 4.5).

The results presented in this section further illustrate that there is a considerable dependence of the band alignment at the CdS/ZnO interface on the details of its preparation. An important factor is the local structure of the ZnO film. There is considerable local disorder when the films are deposited at room temperature in pure Ar, deposition conditions that are often used in thin film solar cells. It is recalled that the disorder is only on a local scale and does not affect the long range order of the films, as obvious from clear X-ray diffraction patterns recorded from such films (see discussion in Sect. 4.2.3.3). Growth of sputter deposited ZnO on CdS always results in an amorphous nucleation layer at the interface. The amorphous nucleation layer affects the valence band offset.

To give an individual value for the band alignment is not possible. Structurally well-ordered interfaces, which are obtained e.g., by deposition of CdS onto ZnO layers deposited at higher temperatures and/or with the addition of oxygen to the sputter gas, show a valence band offset of $\Delta E_{\mathrm{VB}} = 1.2\,\mathrm{eV}$ in good agreement with theoretical calculations [103]. Sputter deposition of undoped ZnO at room temperature in pure Ar onto CdS also leads to a valence band offset of 1.2 eV. In view of the observed dependencies of the band offsets this agreement is fortuitous, as the influence of the local disorder and of the amorphous nucleation layer most likely cancel each other.

The amorphous nucleation layer has the consequence that the Fermi level of the growing ZnO films reaches its equilibrium value already at very low thickness (~2 nm). This is particularly important for ZnO:Al films, where the Fermi level changes by more than 1 eV upon the addition of oxygen to the sputter gas. The amorphous nucleation layer, therefore, substitutes the space charge layer, which is usually necessary for charge equilibration at the interface. This important effect is illustrated in Fig. 4.25.

The absence of large band bendings is also evident for the CdS substrates where the Fermi level is restricted to a narrow energy region in the upper part of the band gap. As there is no (large) bending of the bands in the CdS substrate and in the ZnO film, the band alignment at the interface is mainly determined by the Fermi level in the materials and no longer by the chemical bonds at the interface as in the case of structurally well-ordered interfaces. An important technological consequence of the amorphous nucleation layer is, therefore, that it is essential to control the Fermi level position in the

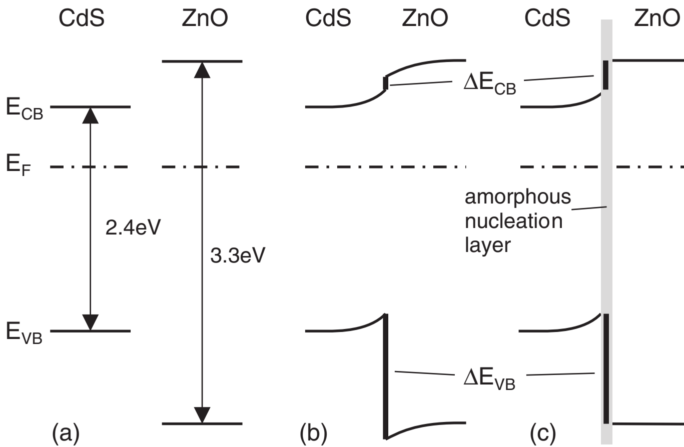

Fig. 4.25. Influence of the amorphous nucleation layer of the ZnO film on the band alignment at a hypothetical CdS/ZnO interface: (**a**) CdS and ZnO before contact; (**b**) in contact with charge equilibrium established by space charge layers; (**c**) in contact with equilibrium established by charges localized in an amorphous ZnO nucleation layer

substrate and in the film to establish a desired band alignment. This might be a reason why chemical bath deposited CdS layers lead to superior solar cells compared with evaporated CdS films. However, Fermi level pinning might also be present in chemical bath deposited CdS films.

The contribution of Fermi level pinning to the band alignment is one of the most important results of the performed studies. It is also very pronounced when CdS is replaced by In_2S_3. Corresponding results are presented in Sect. 4.5.

4.4 The $Cu(In,Ga)Se_2$/ZnO Interface

In principle, a $Cu(In,Ga)Se_2$ thin-film solar cell should be possible without the use of so-called buffer layers like CdS. The necessary p-n junction might be provided by the p-type $Cu(In,Ga)Se_2$ absorber and the n-type TCO. Such a cell structure is also advantageous as it requires less production steps. Consequently, there has been considerable effort to prepare $Cu(In,Ga)Se_2$ thin-film solar cells without a chalcogenide buffer layer (see Chap. 9 of this book and [120]). Conversion efficiencies above 16 % have yet been achieved [121].

For interface studies, it is recommended to use well-defined substrate surfaces. In particular, if the influence of substrate oxidation is investigated, it is essential to use an unoxidized surface. Oxide-free surfaces of $Cu(In,Ga)Se_2$ can be prepared using the decapping procedure, which is described in detail elsewhere [36, 122]. Basically a Se cap layer is deposited onto the $Cu(In,Ga)Se_2$ surface directly after preparation of the layer before the sample is removed from the vacuum system. The cap layer effectively protects the $Cu(In,Ga)Se_2$ surface against oxidation and can be easily removed from the surface by heating at 300°C in the vacuum system at the beginning of the interface experiment. It has been shown that the capping and decapping does not deteriorate the surface as the films allow for preparation of solar cells with the same efficiency as obtained from identically prepared uncapped films [123].

The Se-capped $Cu(In,Ga)Se_2$ films used for the present studies were prepared at the Zentrum für Sonnenenergie und Wasserstoffforschung in Stuttgart, Germany with 30 % of the In substituted by Ga. The films are also used for solar cell preparation and yield an energy conversion efficiency of ∼14 % [36,123]. Good conversion efficiencies are obtained from films, which are prepared with a slight Cu deficiency (∼22 % Cu instead of the nominal 25 % of Cu in stoichiometric chalcopyrites) [124]. Surfaces of such materials are, however, considerably depleted of Cu and show a surface composition that corresponds to the $Cu(In,Ga)_3Se_5$ vacancy compound with a typical Cu concentration of $11 - 13$ % [36, 123, 125]. The importance of this compound for the $Cu(In,Ga)Se_2$ surfaces and interfaces has been pointed out first by Schmid et al. [126, 127].

4.4.1 Chemical Properties

A set of spectra recorded during stepwise deposition of ZnO onto a decapped Cu(In,Ga)Se_2 surface is shown in Fig. 4.26. The ZnO film has been sputtered from an undoped ZnO target using 15 W dc power but otherwise the same "standard" deposition conditions, which have been used for investigation of the CdS/ZnO interface. On a first inspection no changes in the shape of the peaks is observed during deposition. A chemical reaction between Cu(In,Ga)Se_2 and ZnO is, therefore, not evident.

The O 1s spectra do not show the surface species at low coverage in contrast to the CdS/ZnO interface (see Fig. 4.19). The difference has already been discussed in Sect. 4.2.2.2, where the absence of the surface species has been attributed to the propensity of the Cu(In,Ga)Se_2 surface to dissociate oxygen. However, in case the oxygen can easily dissociate on the surface, an

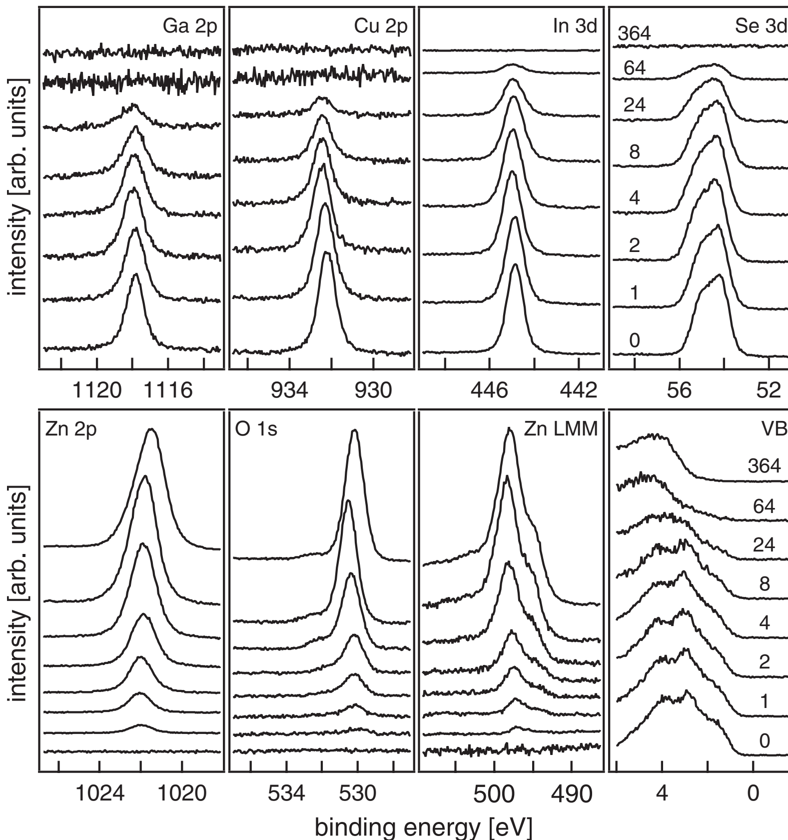

Fig. 4.26. Core levels, Zn LMM Auger level and valence bands recorded using monochromatic Al Kα radiation during sputter deposition of undoped ZnO onto a decapped Cu(In,Ga)Se_2 sample. The deposition times are indicated in seconds

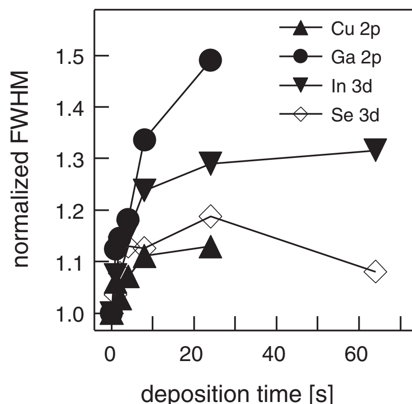

Fig. 4.27. Normalized full widths at half maximum of substrate core levels in dependence on deposition time for the spectra shown in Fig. 4.26

oxidation of the substrate is to be expected. A first indication of a stronger chemical interaction between the deposited ZnO and the Cu(In,Ga)Se_2 surface is provided by the full widths at half maximum (FWHM) of the substrate core-level emissions. These are given in Fig. 4.27. The values are normalized for better comparison. A considerable increase of the FWHM is particularly observed for the Ga 2p and to a lesser extend also for the In 3d level.

The small changes of the Ga and In core levels with changes in chemical environment is well known in surface science. A higher sensitivity to chemical interactions is usually obtained by the Auger levels. The Zn LMM Auger level of the growing ZnO film is included in Fig. 4.26. It shows the same structure independent on ZnO film thickness, indicating no substantial changes in chemical environment. In particular, there is no evidence for the formation of Zn–Se bonds, which are expected at ~2 eV lower binding energies and which have been observed by Loreck et al. for a different absorber composition and interface preparation [128]. Figure 4.28 shows the substrate Auger emissions. No noticeable changes during ZnO growth are observed in the Cu LMM and the Se MNN levels.

A small additional emission occurs at higher binding energy with increasing ZnO thickness in the In MNN level. This is a clear indication for the formation of In–O bonds. An additional emission also grows in the Ga LMM emission. Hence the formation of Ga–O bonds is also indicated. The formation of Ga–O and In–O bonds is thermodynamically favorable compared with Zn–O bonds because of the larger formation enthalpies of Ga_2O_3 (6.15 eV/Ga atom [129]) and In_2O_3 (4.8 eV/In atom [130]) compared with 3.6 eV for ZnO. Nevertheless, the oxidation of the Cu(In,Ga)Se_2 substrate is not very pronounced and limited to the topmost surface layers as estimated from the given spectra.

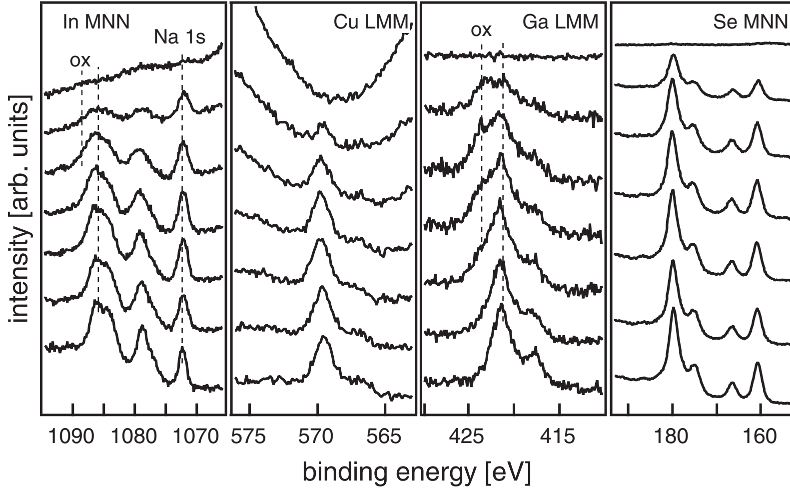

Fig. 4.28. Auger levels recorded using monochromatic Al Kα radiation during sputter deposition of undoped ZnO onto a decapped Cu(In,Ga)Se_2 sample. *Vertical dashed lines* indicate line positions from the clean substrate and from additional components occurring during ZnO deposition. The latter are indicated by "ox." The In MNN spectra also includes the Na 1s signal, which is due to diffusion of Na from the soda lime glass substrate

Chemical interactions at the interface are further reflected in the decay of the substrate emissions with increasing ZnO film thickness. Because of the dependence of the photoelectron escape depth on kinetic energy [31], a faster attenuation of deeper bound levels is to be expected. This contrasts with the experimental observation, which is presented in Fig. 4.29. As expected the slowest attenuation with increasing ZnO deposition is obtained for the Se 3d level, followed by sligthly faster attenuation of the In 3d level. The strongest attenuation is observed for the Cu 2p level and not for Ga 2p as expected from its lower kinetic energy. In general, the fast attenuation of the substrate core levels suggests a layer-by-layer growth mode and no substantial intermixing between the Cu(In,Ga)Se_2 substrate and the ZnO film. Such an intermixing occurs only at higher substrate temperatures [131].

The decay length obtained from fitting exponential curves to the integrated intensities are plotted in the right graph of Fig. 4.29 in dependence on the kinetic energy of the photoelectrons. Escape depths calculated according to the formula given by Tanuma, Powell, and Penn [37] and by Seah and Dench [38] are shown for comparison. The curves are scaled to match the values of the In 3d and Se 3d levels. The decay length of the Cu 2p level is considerably smaller than the theoretical value, while the one of Ga is considerably larger. This suggests that two mechanisms are responsible for the faster attenuation of the Cu 2p compared with the Ga 2p level: (1) a depletion

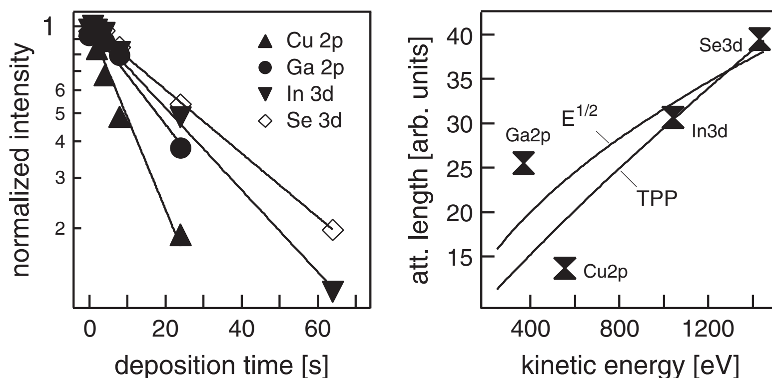

Fig. 4.29. Normalized integrated intensities (*left*) of substrate core levels in dependence on deposition time for the spectra shown in Fig. 4.26. The deposition rate is estimated to be $\sim 2\,\mathrm{nm\,min^{-1}}$. The lines in the *left graph* are obtained by curve fitting of the data to an exponential decay. The derived attenuation times are displayed in the *right graph* in dependence on electron kinetic energy together with theoretical energy-dependent escape depth calculated using the formula by Tanuma, Powell, and Penn [37] and using a $\sqrt{E}$ law [38]

of Cu from the surface and (2) an enrichment of Ga at the surface. The latter might be explained by the formation of the Ga-oxide species, which could lead to some segregation of Ga. The first observation would be in-line with observed Cu depletion at Cu(In,Ga)Se_2 surfaces as a result of interface formation [36,132–136], which is related to an upward shift of the Fermi level [134]. An upward shift of the Fermi level is also observed during deposition of ZnO onto de-capped Cu(In,Ga)Se_2 (see Sect. 4.4.2), supporting this correlation. However, as the Cu(In,Ga)Se_2 surfaces used for this study are already considerably depleted of Cu, a strong further Cu depletion is not expected.

In contrast to the tendency for a Cu depletion in the course of ZnO deposition, Lauermann et al. have reported Cu accumulation at the interface between Cu(In,Ga)$(S,Se)_2$ and rf magnetron sputtered (Zn,Mg)O films [137]. The observation was attributed to the electric field, which is present during the sputter deposition process. For rf sputtering, the electric field at the substrate might be considerably larger than for dc sputtering [138], which is used in the experiment presented in Figs. 4.26–4.29. This difference might explain the discrepancy between the two different experiments. However, also the different substrate composition and preparation as well as other sputter parameters might contribute to the different behavior.

Another species might contribute to the chemistry and electronic properties at the interface. As evident from the In MNN spectra shown in Fig. 4.28, there is also sodium present at the surface. The sodium diffuses from the soda lime glass substrate during deposition of the Cu(In,Ga)Se_2 film and has a beneficial effect on the solar cell conversion efficiency [139]. As mentioned

by Platzer-Björkman et al., the Na content might be directly related to the conversion efficiency of $Cu(In,Ga)Se_2$/ZnO solar cells [140].

The spectra in Fig. 4.28 indicate that the Na 1s core level exhibits a slower attenuation compared with the nearby In MNN Auger level. A comparable behavior has been observed at interfaces between CdS and single crystal $CuInSe_2$ substrates, where Na monolayers have been deliberately inserted by vacuum deposition [133] and also between interfaces of CdS and decapped polycrystalline $Cu(In,Ga)Se_2$ films [141]. Apparently Na is at least partially dissolved in the growing ZnO film. The effect of Na might, therefore, at least partially be related to its influence on the doping of the first ZnO layers. Na may act both as an acceptor and as a donor in ZnO [142]. If Na is predominantly inserted as an acceptor by substituting Zn or as a donor (interstitial Na) depends on the Fermi energy position in the ZnO. At the interface the Fermi energy is close to the conduction band and it is, therefore, more likely that Na is incorporated as an acceptor (see description in Chap. 1). The reduced doping of the ZnO can change the energy band diagram.

4.4.2 Electronic Properties

To determine the valence band offset at the interface, the binding energies of the core levels are plotted in dependence on deposition time in Fig. 4.30. Core

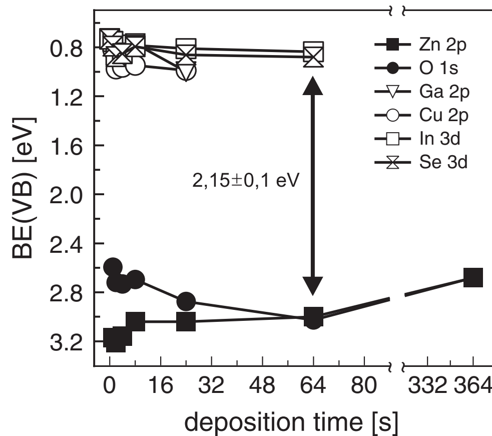

Fig. 4.30. Evolution of valence band maxima in dependence on ZnO deposition time as derived from core-level binding energies of the spectra shown in Fig. 4.29. The ZnO films were deposited by magnetron sputtering from an undoped ZnO target at room temperature using 15 W dc power. Core level to valence band maxima binding energy differences are comparable to those presented in Fig. 4.15 for ZnO and to those given in [36] for $Cu(In,Ga)Se_2$. The different evolution of the Zn 2p and O 1s derived valence band positions for ZnO deposition times indicates the presence of an amorphous nucleation layer, as already discussed in Sect. 4.3.2

level to valence band maximum binding energy differences are determined from the decapped Cu(In,Ga)Se_2 substrate and the thick ZnO film, respectively. The values correspond well with those given recently for Cu(In,Ga)Se_2 [36] and with those in Fig. 4.15 for undoped ZnO films deposited at room temperature in pure Ar.

According to our experience, it is more difficult to determine a reliable valence band offset for the Cu(In,Ga)Se_2/ZnO interface than for the CdS/ZnO interface. This is related to the lower substrate core-level intensities because of the presence of multiple cations. The substrate intensity might, therefore, be already completely suppressed when the Zn 2p and the O 1s derived valence band maxima (see filled circles and squares in Fig. 4.30) reach the same value, and, therefore, reflect a proper ZnO valence band maximum (end of the amorphous nucleation layer). This difficulty is not present in the data set in Fig. 4.30 and for a deposition time of 64 s a valence band offset of $\Delta E_{\mathrm{VB}} = 2.15 \pm 0.1\,\mathrm{eV}$ can be determined. In another experiment, we have derived a slightly smaller valence band offset of $\Delta E_{\mathrm{VB}} = 1.98 \pm 0.2\,\mathrm{eV}$ [70]. The larger uncertainty is due to the above-mentioned difficulties.

The valence band offsets determined in our group are very close to values reported in literature. Platzer-Björkman et al. have determined $\Delta E_{\mathrm{VB}} = 2.2 \pm 0.2\,\mathrm{eV}$ for ALD[10]-ZnO deposited onto $CuInSe_2$ or Cu(In,Ga)Se_2 [143, 144]. Weinhardt et al. give a valence band offset for ILGAR[11]-ZnO on CuIn(S,Se)$_2$ substrates of $\Delta E_{\mathrm{VB}} = 1.8 \pm 0.2\,\mathrm{eV}$ [60]. The comparable values for the different interface preparation and substrate compositions suggest a rather small variation of the band alignment with these parameters.

Figure 4.31 shows ultraviolet photoelectron spectra recorded during the same interface experiment shown in Fig. 4.26. A clear transition from the Cu(In,Ga)Se_2 valence band structure with a valence band maximum at $\sim$0.8 eV binding energy to the ZnO valence band structure with a valence band maximum at $\sim$3 eV is observed with increasing ZnO deposition. The well-resolved valence band features are enabled by the in situ sample preparation. Also very sharp secondary electron cutoffs are obtained, which allow for an accurate determination of work functions. The work functions of Cu(In,Ga)Se_2 and ZnO are determined as 5.4 and 4.25 eV, respectively. These result in ionization potentials of 6.15 and 7.15 eV for Cu(In,Ga)Se_2 and ZnO.

The ionization potential of ZnO is slightly larger than the one usually obtained for such deposition conditions, which lead to a predominant (0001) Zn-terminated surface. The deviation is, however, directly explained by the microstructure of the film (see Fig. 4.21). At low coverage the (0001) orientation of the grains is not yet fully developed and a statistical orientation should lead to a larger ionization potential. The evolution of the orientation of the ZnO grains is reflected in the strong shift of the secondary electron cutoff for deposition times $\geq$8 s. At this coverage the ZnO valence band structure is

[10] Atomic layer deposition.
[11] Ion layer gas reaction.

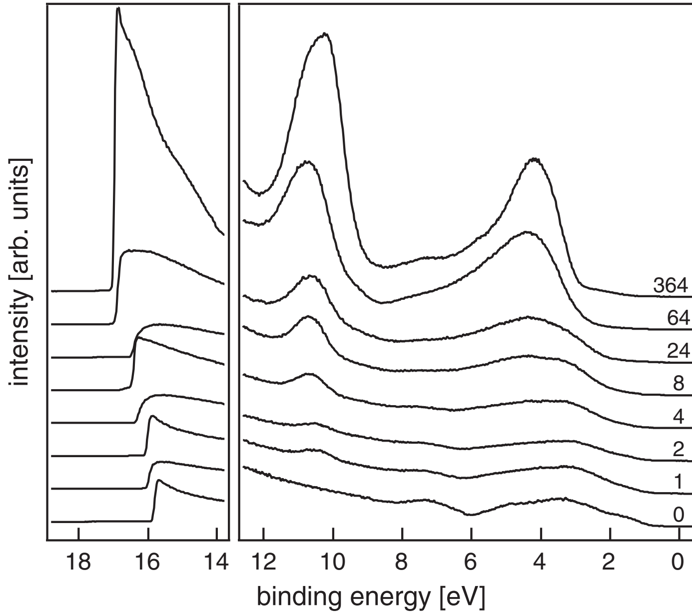

Fig. 4.31. UPS valence bands recorded during deposition of undoped ZnO onto decapped Cu(In,Ga)Se_2 showing the valence band structure (*right*) and the secondary electron cutoff (*left*). The deposition times are indicated in seconds

almost completely developed but the work function still amounts to ∼4.8 eV. An energy band diagram of the Cu(In,Ga)Se_2/ZnO interface is shown in Fig. 4.32.

The band alignment at the Cu(In,Ga)Se_2/ZnO interface can be compared with the band alignment expected for Cu(In,Ga)Se_2/CdS/ZnO sequence. The valence band offset at the CdS/ZnO interface is taken as $\Delta E_{\mathrm{VB}} = 1.2\,\mathrm{eV}$, which is obtained for the same ZnO deposition conditions as those used in the investigation of the Cu(In,Ga)Se_2/ZnO interface. The valence band offset at the Cu(In,Ga)Se_2/CdS interface is taken from literature [36, 106, 123, 125]. In the corresponding studies identically prepared decapped Cu(In,Ga)Se_2 substrates have been used. CdS was deposited by thermal evaporation as also applied in the studies of the CdS/ZnO interface formation. The transitivity of the band alignment in the Cu(In,Ga)Se_2/CdS/ZnO sequence is excellently fulfilled as evident from Fig. 4.33. This indicates that a modification of the band alignment by the introduction of the CdS buffer layer does not account for the superior conversion efficiencies typically obtained with CdS buffer layers. However, the high efficiencies are obtained with chemical bath deposited and not with evaporated CdS buffer layers. So far, Cu(In,Ga)Se_2 thin-film solar cells with a direct contact between the absorber and the TCO have achieved higher efficiencies than solar cells with evaporated CdS buffer layers [112, 120].

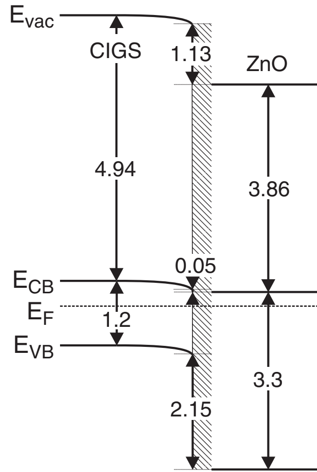

Fig. 4.32. Energy band diagram of the Cu(In,Ga)Se_2/ZnO interface as determined from photoelectron spectroscopy. The *shaded region* indicates the amorphous nucleation layer of the ZnO film

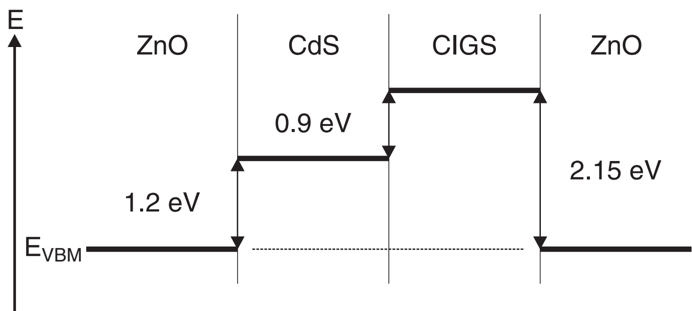

Fig. 4.33. Energetic positions of valence band maxima in the Cu(In,Ga)Se_2/CdS/ZnO sequence showing the transitivity of band alignment. The valence band offsets for CdS/ZnO and Cu(In,Ga)Se_2/ZnO are discussed in this chapter. The valence band offset for the Cu(In,Ga)Se_2/CdS interface is taken from literature [36, 106, 123, 125]

4.5 The In_2S_3/ZnO Interface

4.5.1 Cu(In,Ga)Se_2 Solar Cells with In_2S_3 Buffer Layers

In_2S_3 or In_2S_3 containing compounds are possible alternatives for the CdS buffer layer in Cu(In,Ga)Se_2 thin-film solar cells [120, 145–148]. The In_2S_3 layers are prepared by various techniques as chemical bath deposition [145], thermal evaporation [146], atomic layer deposition (ALD) [147], and magnetron sputtering [148]. Energy conversion efficiencies above 16 % have been

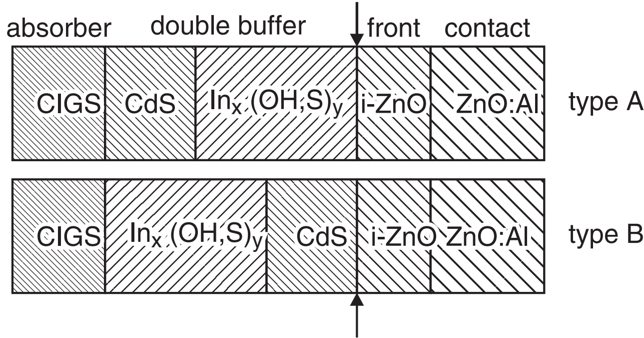

Fig. 4.34. Schematic arrangement of buffer layers used in the experiments carried out by Nguyen et al. [154, 155]

reached [147]. Depending on deposition technique and conditions In_xS_y shows a variety of compositions and structures [149]. The In–S phase diagram is given by Godecke and Schubert [150]. Here we present results using In_2S_3 layers prepared by thermal evaporation of the In_2S_3 compound. The substrates were held at room temperature or at 250°C during deposition. Using optical transmission we have determined an optical gap of the films of $E_g = 1.9$ eV [107]. This value is smaller than the optical gap of $E_g = 2.75$ eV determined by Spiering et al. for ALD-In_2S_3 [151] but agrees well with optical gaps of $E_g = 1.98$ eV or 2.0–2.2 eV determined for MOCVD In_2S_3 films by Nomura et al. [152] and for evaporated films by Timoumi et al. [153].

A particular buffer layer experiment, carried out by Nguyen et al. [154, 155], is shown in Fig. 4.34. Two different combinations of chemical bath deposited CdS and $In_x(OH,S)_y$ buffer layers were used to fabricate $Cu(In,Ga)Se_2$ thin-film solar cells. The experiment was defined in order to identify the interface that leads to poor efficiencies if single $In_x(OH,S)_y$ buffer layers are used. The type A arrangement of the two buffer layers with a $Cu(In,Ga)Se_2$/CdS and an $In_x(OH,S)_y$/ZnO interface results in poor efficiencies, while type B arrangement with a $Cu(In,Ga)Se_2/In_x(OH,S)_y$ and a CdS/ZnO interface results in a high efficiency. This observation strongly suggests that the interface between $In_x(OH,S)_y$ and ZnO limits the efficiency.

4.5.2 Chemical Properties

X-ray photoelectron spectra recorded during interface formation of magnetron sputtered Al-doped ZnO with an evaporated In_2S_3 substrate are shown in Fig. 4.35. The In_2S_3 substrate has been deposited at 250°C substrate temperature and the ZnO:Al was deposited at room temperature in pure Ar, resulting in a degenerately doped film. The valence band maximum after the last deposition step (not shown) is at $E_F - E_{VB} = 3.9 \pm 0.1$ eV.

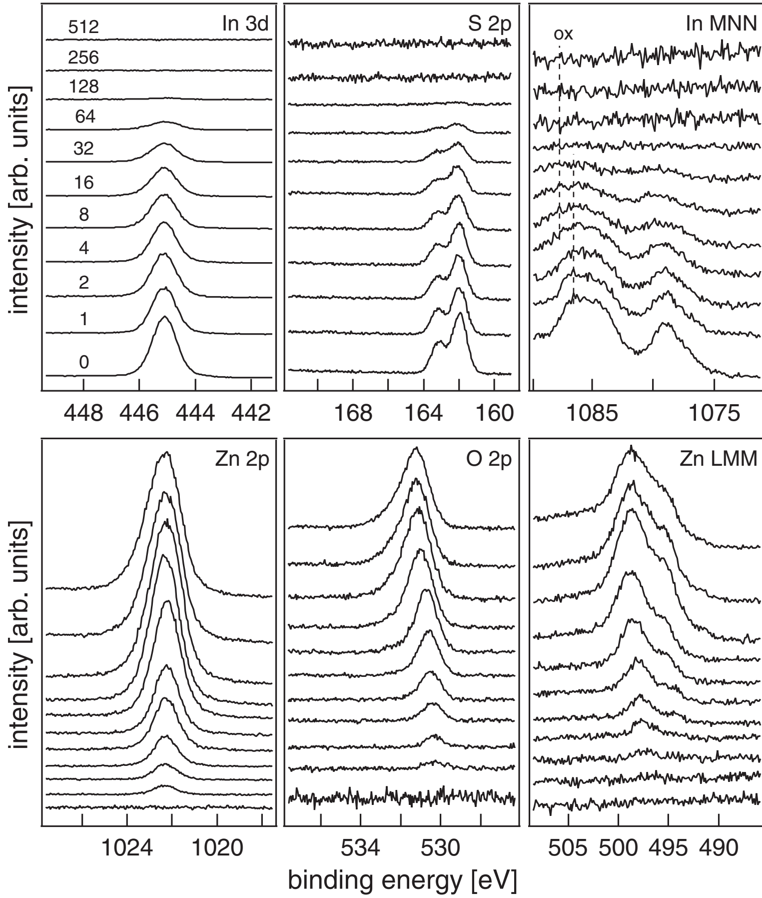

Fig. 4.35. Core levels and cation Auger levels of an In_2S_3 substrate during sputter deposition of Al-doped ZnO (experiment ISZA-B). The deposition times are indicated in seconds. In_2S_3 was deposited at 250°C and ZnO:Al at room temperature in pure Ar. Reproduced with permission from [136]

Degenerate doping is further indicated by the broad structure of the Zn LMM Auger line after the last deposition step (compare Sect. 4.2.2).

From the core level and Zn LMM Auger level shown in Fig. 4.35 no chemical reactions at the interface are evident. However, the In MNN Auger level shows an additional emission at higher binding energy with increasing ZnO deposition. Compared with the deposition of ZnO onto Cu(In,Ga)Se_2 (Fig. 4.28), the oxidation of the In is more pronounced. The O 1s level shows no high binding energy species at low coverage, as also observed for the Cu(In,Ga)Se_2 substrate (Fig. 4.26). According to the discussion in Sect. 4.2.2.2, this indicates that the In_2S_3 surface facilitates oxygen

dissociation. This observation concurs well with substrate oxidation observed in the In MNN Auger level.

Interface formation between In_2S_3 substrates and ZnO:Al has also been studied with 10 % oxygen added to the sputter gas during ZnO:Al deposition. Corresponding X-ray photoelectron spectra are shown in Fig. 4.36. The In_2S_3 substrate has been deposited at 250°C substrate temperature and the ZnO:Al was deposited at room temperature. This results in a highly compensated film. The valence band maximum after the last deposition step (not shown) is at $E_F - E_{VB} = 2.7 \pm 0.1$ eV. A low doping of the films is further indicated by the sharper features of the Zn LMM Auger line after the last deposition step compared with the spectra obtained for the highly doped film in Fig. 4.35.

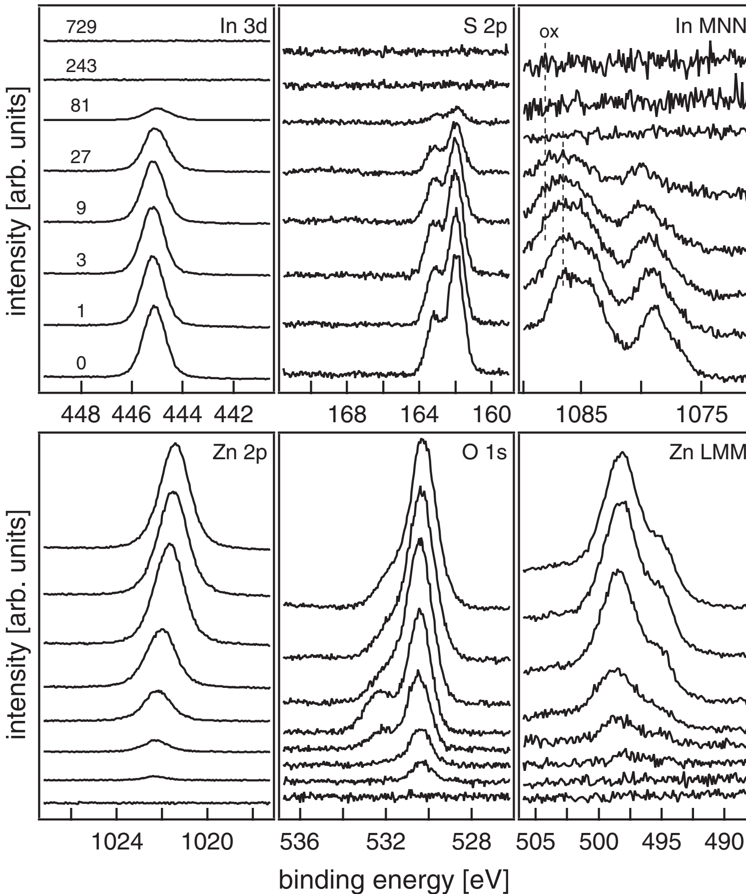

Fig. 4.36. Core levels and cation Auger levels of an In_2S_3 substrate during sputter deposition of Al-doped ZnO (experiment ISZA-C). The deposition times are indicated in seconds. In_2S_3 was deposited at 250°C and ZnO:Al at room temperature in a sputter gas containing 10 % O_2

Again no evident chemical changes in the core level and Zn LMM Auger emissions are observed during ZnO deposition. The broadening of the In MNN Auger line is ascribed to the substrate oxidation. Compared with the interface where ZnO has been deposited without oxygen in the sputter gas, the broadening of the In MNN Auger level is not more pronounced. Hence, substrate oxidation is not enhanced when oxygen is added to the sputter gas. This further supports the conclusion that substrate oxidation is not governed by the energy of the deposited particles but rather by the ability of the substrate surface to dissociate oxygen.

Interface formation between In_2S_3 and ZnO has also been studied for the reverse deposition sequence with Al-doped ZnO films used as substrates [70]. In this case, only degenerately doped substrates were used. Photoemission spectra indicate no chemical reactivity at the surface.

4.5.3 Electronic Properties

The valence band offsets between In_2S_3 and ZnO are determined from the substrate and overlayer core-level binding energies in dependence on deposition time. Core-level binding energies with respect to the valence band maximum are determined from the substrate and the thick overlayer, respectively. The values for ZnO:Al are within the experimental uncertainty of ± 0.1 eV the same as those presented in Fig. 4.15. Values for In_2S_3 films deposited at room temperature are 443.7 ± 0.1 eV for In 3d and 160.4 ± 0.1 eV for S 2p, respectively. Values for In_2S_3 films deposited at 250°C are 444.0 ± 0.1 eV for In 3d and 160.85 ± 0.1 eV for S 2p, respectively. The difference between the films deposited at different substrate temperatures indicates a significant change in the density of states, which could be related to a different composition and/or structure of the films. However, In 3d to S 2p intensity ratios for In_2S_3 films deposited at room temperature and at 250°C are not significantly different. Therefore, structural differences most likely account for the variation of the core-level binding energies with respect to the valence band maximum. It has to be expected that the structural differences also affect the band gaps of the In_2S_3 films. Band gaps were so far only determined for the films deposited at room temperature [107].

The valence band offsets between In_2S_3 and ZnO:Al determined from Fig. 4.37 are $\Delta E_{VB} = 2.78 \pm 0.2$ eV and $\Delta E_{VB} = 1.86 \pm 0.2$ eV for the interface with degenerately doped and with oxygen compensated low doped ZnO:Al, respectively. There is almost no change of the valence band maximum binding energy in the substrate in the course of ZnO:Al deposition. No band bending is, therefore, introduced in the substrate by contact formation. As both substrates show comparable Fermi level positions, only the different Fermi level positions in the ZnO:Al films account for the different valence band offsets. This situation is comparable to those observed at the CdS/ZnO:Al interface (see left graph in Fig. 4.24). However, the Fermi level in In_2S_3 changes even less than in CdS. Therefore, the difference in ΔE_{VB}

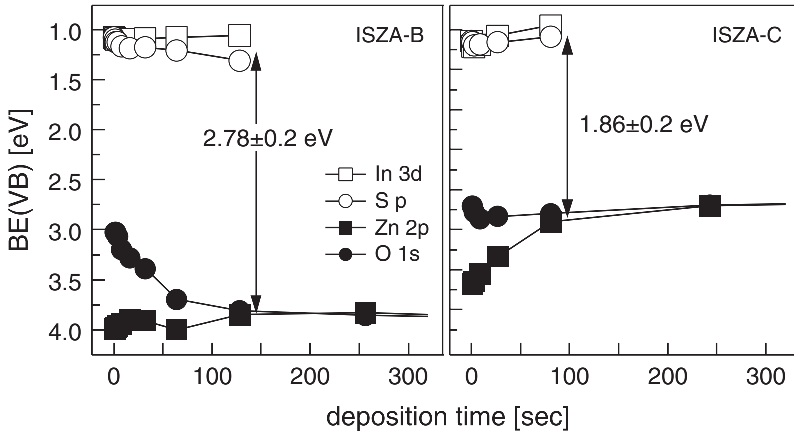

Fig. 4.37. Evolution of valence band maxima of In_2S_3 and ZnO:Al for the two experiments displayed in Figs. 4.35 (*left*) and 4.36 (*right*). The difference between the curves derived from the Zn 2p and O 1s level at low coverage indicates the presence of an amorphous nucleation layer. Reproduced with permission from [136]

between In_2S_3 and highly doped or low doped ZnO:Al amounts to ~0.9 eV, which is considerably larger than for CdS (~0.4 eV). The larger difference is a result of the stronger Fermi level pinning in In_2S_3 compared with CdS.

Energy band diagrams for different In_2S_3/ZnO and ZnO/In_2S_3 interfaces are summarized in Fig. 4.38. Vacuum energies are not included, as no UPS was available during the experiments. Hence, it was not possible to determine work functions and ionization potentials for the deposited films. Interface dipole potentials can, however, be estimated using ionization potentials of 7.1 eV for ZnO:Al according to Sect. 4.2.3.2 and an identical value for In_2S_3 [107]. This results in interface dipole potentials of 1.8–2.8 eV for the different investigated interfaces. These large values indicate a considerable density of states at the interface, which would explain the strong influence of the In_2S_3/ZnO interface on the solar cell performance [154, 155].

The largest difference in valence band offset is observed for the two experiments presented in detail above. Valence band offsets for the other three interfaces are very similar and amount to 2.3–2.4 eV. All three interfaces leading to this valence band offset are prepared using the same deposition conditions: ZnO:Al deposition at room temperature in pure Ar leading to degenerately doped ZnO:Al and In_2S_3 deposition at room temperature. The difference in ΔE_{VB} compared with the interface in which In_2S_3 has been deposited at 250°C substrate temperature (the second diagram from the left in Fig. 4.38) is the different Fermi energy position in the In_2S_3 film.

For all investigated interfaces the valence band offset can be estimated by the alignment of the Fermi levels of thick In_2S_3 and ZnO:Al prepared under the same conditions used in the interface experiment. This is related to the very small band bending observed at the interfaces (≤0.2 eV) and concurs

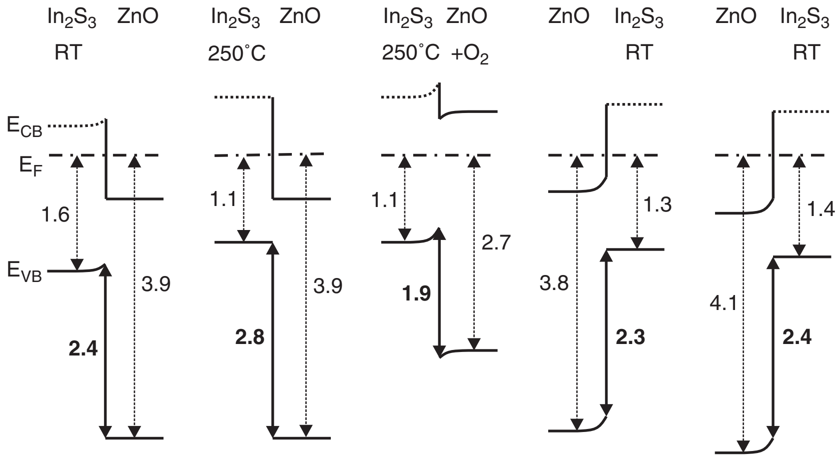

Fig. 4.38. Energy band diagrams at In_2S_3/ZnO interfaces as determined from photoelectron spectroscopy. The material used as substrate during interface formation is shown to the left. In_2S_3 films were deposited by evaporation onto substrates held either at room temperature or at 250°C. ZnO:Al films were prepared by dc magnetron sputtering at room temperature in pure Ar or with 10 % O_2 in the sputter gas as indicated at the top. All values are given in electronvolt. Band bending at the interface is $\leq$0.2 eV in all experiments. Because of the uncertainty in the band gap, the conduction band positions of In_2S_3 are given as *dotted lines*. Reproduced with permission from [136]

well with the large dipole potentials. The behavior is illustrated in the top part of Fig. 4.39.

Figure 4.39 also shows the alignment of valence bands at $CuGaSe_2$/CdS/-ZnO:Al and $CuGaSe_2$/In_2S_3/ZnO:Al interfaces. $CuGaSe_2$ was chosen as no experimental determination of the band alignment between Cu(In,Ga)Se_2 and In_2S_3 is available. For the determination of the valence band offset at the $CuGaSe_2$/CdS and $CuGaSe_2$/In_2S_3 interface the respective contact materials were evaporated at room temperature onto decapped $CuGaSe_2$ surfaces [106, 107]. The valence band offsets at the CdS/ZnO:Al and In_2S_3/ZnO:Al are taken from this chapter for deposition of the ZnO:Al films at room temperature in pure Ar. A deviation of the valence band offsets from transitivity of ∼0.6 eV is evident. The deviation can be attributed to the Fermi level pinning at the In_2S_3/ZnO interface.

Of the energy band diagrams given in Fig. 4.38, the band alignment most suitable for the Cu(In,Ga)Se_2 thin-film solar cell is provided by the interface with the smallest valence band offset (middle diagram). Irrespective of the uncertainty in the In_2S_3 band gap, this alignment has the smallest conduction band offset and hence the largest separation between the In_2S_3 valence band maximum and the ZnO conduction band minimum. This situation should be favorable with respect to the suppression of recombination

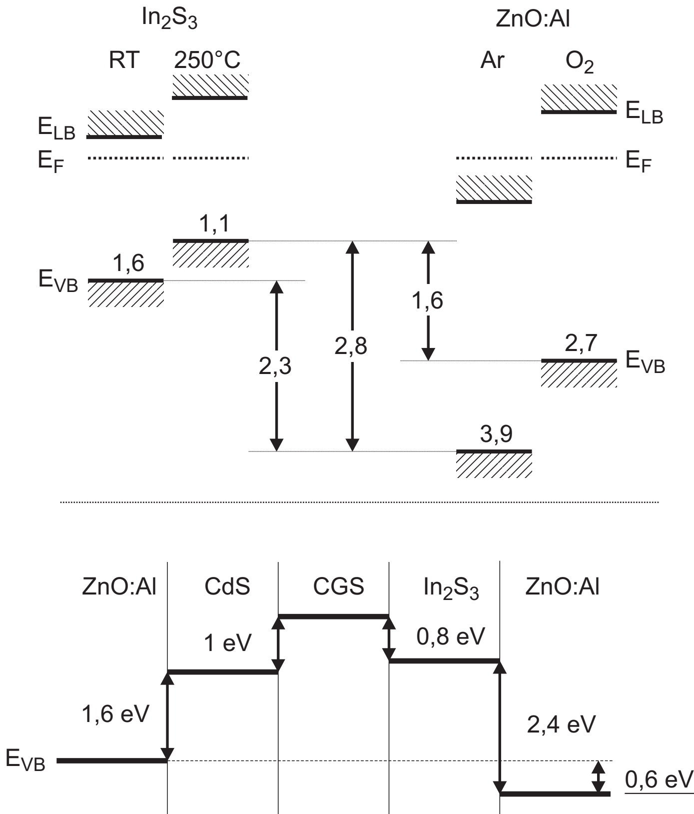

Fig. 4.39. *Top*: Estimation of band alignment (*middle section*) from the Fermi level positions measured at the surfaces of thick In_2S_3 and ZnO:Al films in dependence on deposition conditions.
Bottom: Energy level alignment in the system $CuGaSe_2$-In_2S_3-CdS-ZnO:Al. Valence band offsets for CdS/ZnO:Al and In_2S_3/ZnO:Al are taken from the results presented in this Chap. for ZnO:Al films deposited at room temperature in pure Ar. Valence band offsets for $CuGaSe_2$/CdS and $CuGaSe_2$/In_2S_3 are taken from literature [106, 107]

at the In_2S_3/ZnO interface. In addition, the smallest conduction band offset also allows for larger open circuit voltages [156]. Hence, better solar cell efficiencies are expected for a In_2S_3 deposition temperature around 250°C and the use of undoped ZnO films. This expectation agrees well with the preparation conditions for optimized Cu(In,Ga)Se_2 solar cells applying In_2S_3 buffer layers [146, 148].

Acknowledgement. The work presented here was supported by the German Federal Ministry of Education and Research (BMBF) in the framework of the ZnO

network project (project No. 01SF0034). The discussions and collaborations with the contributing groups permanently stimulated this work. Our work would not have been possible without the continuous support and encouragement by Wolfram Jaegermann, head of the surface science group in Darmstadt. We further acknowledge the experimental contributions of Frauke Rüggeberg, Dr. Gutlapalli Venkata Rao, Christoph Körber, and Juan Angel Sans. We also thank Robert Kniese and Michael Powalla from Zentrum für Sonnenenergie und Wasserstoffforschung for providing the Se-capped Cu(In,Ga)Se_2 thin films.

References

1. S.M. Sze, *Physics of Semiconductor Devices*, 2nd edn. (Wiley, New York, 1981)
2. W. Mönch, *Electronic Properties of Semiconductor Interfaces* (Springer, Berlin Heidelberg New York, 2003)
3. A. Franciosi, C.G. van de Walle, Surf. Sci. Rep. **25**, 1 (1996)
4. M. Peressi, N. Binggeli, A. Baldereschi, J. Phys. D **31**, 1273 (1998)
5. E.T. Yu, J.O. McCaldin, T.C. McGill, Solid State Phys. **46**, 1 (1992)
6. R.T. Tung, J. Vac. Sci. Technol. B **11**, 1546 (1993)
7. H. Kroemer, J. Vac. Sci. Technol. B **11**, 1354 (1993)
8. F. Capasso, G. Margaritondo (eds.), *Heterojunction Band Discontinuities* (North-Holland, Amsterdam, 1987)
9. V. Heine, Phys. Rev. **138**, 1689 (1965)
10. S.G. Louie, J.R. Chelikowsky, M.L. Cohen, Phys. Rev. B **15**, 2154 (1977)
11. S. Kurtin, T.C. McGill, C.A. Mead, Phys. Rev. Lett. **22**, 1433 (1969)
12. K. Ip, G.T. Thaler, H. Yang, S.Y. Han, Y. Li, D.P. Norton, S.J. Pearton, S. Jang, F. Ren, J. Cryst. Growth **287**, 149 (2006)
13. J.H. Lim, S.J. Park, in *Zinc Oxide: Bulk, Thin Films and Nanostructures*, ed. by C. Jagadish, S.J. Pearton (Elsevier, Oxford, 2006), pp. 267–283
14. U. Rau, H.W. Schock, Appl. Phys. A **69**, 131 (1999)
15. M.A. Contreras, B. Egaas, K. Ramanathan, J. Hiltner, A. Swartzlander, F.A. Hasoon, R. Noufi, Prog. Photovolt. Res. Appl. **7**, 311 (1999)
16. P.H.L. Notten, J.E.A.M. van den Meerakker, J.J. Kelly, *Etching of III-V Semiconductors: An Electrochemical Approach* (Elsevier, Oxford, 1991)
17. R. Hannemann, A. Mariano, J. Appl. Phys. **34**, 384 (1963)
18. R. Wiesendanger, H.J. Güntherodt (eds.), *Scanning Tunneling Microscopy*, vol. I–III, 2nd edn. (Springer, Berlin Heidelberg New York, 1996)
19. C.S. Jiang, F.S. Hasoon, H.R. Moutinho, H.A. Al-Thani, M. Romero, M.M. Al-Jassim, Appl. Phys. Lett. **82**, 127 (2003)
20. H. Moormann, D. Kohl, G. Heiland, Surf. Sci. **80**, 261 (1979)
21. K. Winer, L. Ley, Phys. Rev. B **36**, 6072 (1987)
22. R.C. Neville, C.A. Mead, J. Appl. Phys. **43**, 4657 (1972)
23. M. Igalson, H.W. Schock, J. Appl. Phys. **80**, 5765 (1996)
24. H.L. Tuller, J. Electroceram. **4**, 33 (1999)
25. F. Greuter, G. Blatter, Semicond. Sci. Technol. **5**, 111 (1990)
26. J.H. Werner, K. Ploog, H.J. Queisser, Phys. Rev. Lett. **57**, 1080 (1986)
27. M. Turcu, I.M. Kötschau, U. Rau, J. Appl. Phys. **91**, 1391 (2002)
28. K. Nishi, H. Ohyama, T. Siuzuki, T. Mitsuyu, T. Tomimasu, Appl. Phys. Lett. **70**, 3585 (1997)

29. L.J. Brillson, S. Chang, J. Shaw, R.E. Viturro, Vacuum **41**, 1016 (1990)
30. M.J. Hetzer, Y.M. Strzhemechny, M. Gao, M.A. Contreras, A. Zunger, L.J. Brillson, Appl. Phys. Lett. **86**, 162105 (2005)
31. D. Briggs, M.P. Seah, *Practical Surface Analysis by Auger and X-Ray Photoelectron Spectroscopy* (Wiley, New York, 1983)
32. S. Hüfner, *Photoelectron Spectroscopy* (Springer, Berlin Heidelberg New York, 1995)
33. J.R. Waldrop, R.W. Grant, S.P. Kowalczyk, E.A. Kraut, J. Vac. Sci. Technol. A **3**, 835 (1985)
34. W. Jaegermann, A. Klein, C. Pettenkofer, in *Electron Spectroscopies Applied to Low-Dimensional Materials*, ed. by H.I. Hughes, H.P. Starnberg, Physics and Chemistry of Materials with Low-Dimensional Structure (Kluwer, Dordrecht, 2000), pp. 317–402
35. K. Durose, S.E. Asher, W. Jaegermann, D. Levi, B.E. McCandless, W. Metzger, H. Moutinho, P.D. Paulson, C.L. Perkins, J.R. Sites, G. Teeter, M. Terheggen, Prog. Photovolt. Res. Appl. **12**, 177 (2004)
36. A. Klein, T. Schulmeyer, in *Wide Gap Chalcopyrites*, ed. by S. Siebentritt, U. Rau (Springer, Berlin Heidelberg New York, 2006)
37. S. Tanuma, C.J. Powell, D.R. Penn, Surf. Interface Anal. **17**, 927 (1991)
38. M.P. Seah, W.A. Dench, Surf. Interface Anal. **1**, 2 (1979)
39. H.L. Hartnagel, A.L. Dawar, A.K. Jain, C. Jagadish, *Semiconducting Transparent Thin Films* (Institute of Physics Publishing, Bristol, 1995)
40. O. Dulub, L.A. Boatner, U. Diebold, Surf. Sci. **519**, 201 (2002)
41. U. Diebold, L.V. Koplitz, O. Dulub, Appl. Surf. Sci. **237**, 336 (2004)
42. W. Mönch, *Semiconductor Surfaces and Interfaces* (Springer, Berlin Heidelberg New York, 1993)
43. G. Chiarotti (ed.), *Physics of Solid Surfaces, Landolt-Börnstein, Numerical Data and Functional Relationships in Science and Technology, NS III 24a* (Springer, Berlin Heidelberg New York, 1993)
44. C. Noguera, J. Phys. Condens. Matter **12**, R367 (2000)
45. G. Kresse, O. Dulub, U. Diebold, Phys. Rev. B **68**, 245409 (2003)
46. O. Dulub, U. Diebold, G. Kresse, Phys. Rev. Lett. **90**, 016102 (2003)
47. A. Wander, F. Schedin, P. Steadman, A. Norris, R. McGrath, T.S. Turner, G. Thornton, N.M. Harrison, Phys. Rev. Lett. **86**, 3811 (2001)
48. B. Meyer, D. Marx, Phys. Rev. B **67**, 035403 (2003)
49. M. Kunat, S.G. Girol, T. Becker, U. Burghaus, C. Wöll, Phys. Rev. B **66**, 081402 (2002)
50. D.J. Chadi, Phys. Rev. Lett. **52**, 1911 (1984)
51. M. Moll, A. Kley, E. Pehlke, M. Scheffler, Phys. Rev. B **54**, 8844 (1996)
52. K.W. Haberern, M.D. Pashley, Phys. Rev. B **41**, 3226 (1990)
53. S.C. Chang, P. Mark, J. Vac. Sci. Technol. **12**, 629 (1975)
54. D.K. Biegelsen, R.D. Bringans, J.E. Northrup, L.E. Swartz, Phys. Rev. Lett. **65**, 452 (1990)
55. R.G. Egdell, J. Rebane, T.J. Walker, D.S.L. Law, Phys. Rev. B **59**, 1792 (1999)
56. R.G. Egdell, T.J. Walker, G. Beamson, J. Electron Spectrosc. **128**, 59 (2003)
57. V. Christou, M. Etchells, O. Renault, P.J. Dobson, O.V. Salata, G. Beamson, R.G. Egdell, J. Appl. Phys. **88**, 5180 (2000)
58. Y. Gassenbauer, R. Schafranek, A. Klein, S. Zafeiratos, M. Hävecker, A. Knop-Gericke, R. Schlögl, Phys. Rev. B **73**, 245312 (2006)

59. G. Venkata Rao, A. Klein, (unpublished results)
60. L. Weinhardt, M. Bär, H.J. Muffler, C.H. Fischer, M.C. Lux-Steiner, T.P. Niesen, F. Karg, T. Gleim, C. Heske, E. Umbach, Thin Solid Films **431–432**, 272 (2003)
61. L. Jing, Z. Xu, X. Sun, J. Shang, W. Cai, Appl. Surf. Sci. **180**, 308 (2001)
62. M. Kunat, S.G. Girol, U. Burghaus, C. Wöll, J. Phys. Chem. B **107**, 14350 (2003)
63. G. Schön, J. Electron Spectrosc. **2**, 75 (1973)
64. G.E. Hammer, R.M. Shemenski, J. Vac. Sci. Technol. A **1**, 1026 (1983)
65. M.N. Islam, T.B. Ghosh, K.L. Chopra, H.N. Acharya, Thin Solid Films **280**, 20 (1996)
66. J.F. Chang, W.C. Lin, M.H. Hon, Appl. Surf. Sci. **183**, 18 (2001)
67. T. Becker, M. Kunat, C. Boas, U. Burghaus, C. Wöll, J. Chem. Phys. **113**, 6334 (2000)
68. M. Chen, Z.L. Pei, C. Sun, L.S. Wen, X. Wang, J. Cryst. Growth **220**, 254 (2000)
69. F. Stucki, P. Brüesch, F. Greuter, Surf. Sci. **189–190**, 294 (1987)
70. F. Säuberlich, Ph.D. thesis, Technische Universität Darmstadt (Mensch und Buch, Berlin, 2006)
71. G. Venkata Rao, F. Säuberlich, A. Klein, Appl. Phys. Lett. **87**, 032101 (2005)
72. P. Erhart, A. Klein, K. Albe, Phys. Rev. B **72**, 085213 (2005)
73. P. Erhart, K. Albe, A. Klein, Phys. Rev. B **73**, 205203 (2006)
74. K. Ellmer, J. Phys. D Appl. Phys. **33**, R17 (2000)
75. A. Zangwill, *Physics at Surfaces* (Cambridge University Press, Cambridge, 1988)
76. R.K. Swank, Phys. Rev. **153**, 844 (1967)
77. H. Moormann, D. Kohl, G. Heiland, Surf. Sci. **100**, 302 (1980)
78. W. Göpel, U. Lampe, Phys. Rev. B **22**, 6447 (1980)
79. K. Jacobi, G. Zwicker, A. Gutmann, Surf. Sci. **141**, 109 (1984)
80. C.T. Campbell, K.A. Daube, J.M. White, Surf. Sci. **182**, 458 (1987)
81. V.E. Henrich, P.A. Cox, *The Surface Science of Metal Oxides* (Cambridge University Press, Cambridge, 1994)
82. U. Meier, Ph.D. thesis, BTU Cottbus (2003)
83. C. Agashe, O. Kluth, J. Hüpkes, U. Zastrow, B. Rech, M. Wuttig, J. Appl. Phys. **95**, 1911 (2004)
84. H. Fujiwara, M. Kondo, Phys. Rev. B **71**, 075109 (2005)
85. I. Ivanov, J. Pollmann, Phys. Rev. B **24**, 7275 (1981)
86. R. Dorn, H. Lüth, M. Büchel, Phys. Rev. B **16**, 4675 (1977)
87. S. Brehme, F. Fenske, W. Fuhs, E. Nebauer, M. Poschenrieder, B. Selle, H. Sieber, Thin Solid Films **342**, 167 (1999)
88. J.H. Hwang, D.D. Edwards, D.R. Kammler, T.O. Mason, Solid State Ionics **129**, 135 (2000)
89. S.P. Harvey, T.O. Mason, Y. Gassenbauer, R. Schafranek, A. Klein, J. Phys. D Appl. Phys. **39**, 3959 (2006)
90. F. Säuberlich, J. Fritsche, R. Hunger, A. Klein, Thin Solid Films **431–432**, 378 (2003)
91. W. Ranke, Phys. Rev. B **27**, 7807 (1983)
92. J. Fritsche, D. Kraft, A. Thissen, T. Mayer, A. Klein, W. Jaegermann, Mater. Res. Soc. Symp. Proc. **668**, H6.6 (2001)

93. T. Löher, A. Klein, Y. Tomm, C. Pettenkofer, W. Jaegermann, Semicond. Sci. Technol. **15**, 1 (2000)
94. R. Cebulla, R. Wendt, K. Ellmer, J. Appl. Phys. **83**, 1087 (1998)
95. G.J. Exarhos, S.K. Sharma, Thin Solid Films **270**, 27 (1995)
96. I. Sieber, N. Wanderka, I. Urban, I. Dörfel, E. Schierhorn, F. Fenske, W. Fuhs, Thin Solid Films **330**, 108 (1998)
97. E. Mirica, G. Kowach, P. Evans, H. Du, Cryst. Growth Des. **4**, 147 (2004)
98. P. Schröer, P. Krüger, J. Pollmann, Phys. Rev. B **47**, 6971 (1993)
99. C. McGuinness, C.B. Stagarescu, P.J. Ryan, J.E. Downes, D. Fu, K.E. Smith, R.G. Egdell, Phys. Rev. B **68**, 165104 (2003)
100. C.L. Dong, C. Persson, L. Vayssieres, A. Augustsson, T. Schmitt, M. Mattesini, R. Ahuja, C.L. Chang, J.H. Guo, Phys. Rev. B **70**, 195325 (2004)
101. I. Hamberg, C.G. Granqvist, J. Appl. Phys. **60**, R123 (1986)
102. M. Ruckh, D. Schmid, H.W. Schock, J. Appl. Phys. **76**, 5945 (1994)
103. S.H. Wei, A. Zunger, Appl. Phys. Lett. **72**, 2011 (1998)
104. R. Klenk, Thin Solid Films **387**, 135 (2001)
105. M. Gloeckler, A.L. Fahrenbruch, J.R. Sites, in *Proceedings of the 3rd World Conference on Photovoltaic Solar Energy Conversion*, Osaka, Japan, 2003, p. 2P.D3.52
106. T. Schulmeyer, R. Kniese, R. Hunger, W. Jaegermann, M. Powalla, A. Klein, Thin Solid Films **451–452**, 420 (2004)
107. T. Schulmeyer, A. Klein, R. Kniese, M. Powalla, Appl. Phys. Lett. **85**, 961 (2004)
108. B. Späth, J. Fritsche, F. Säuberlich, A. Klein, W. Jaegermann, Thin Solid Films **480–481**, 204 (2005)
109. J. Fritsche, A. Klein, W. Jaegermann, Adv. Eng. Mater. **7**, 914 (2005)
110. T.M. Duc, C. Hsu, J.P. Faurie, Phys. Rev. Lett. **58**, 1127 (1987)
111. E.T. Yu, M.C. Phillips, J.O. McCaldin, T.C. McGill, J. Vac. Sci. Technol. B **9**, 2233 (1991)
112. M. Rusu, T. Glatzel, A. Neisser, C.A. Kaufmann, S. Sadewasser, M.C. Lux-Steiner, Appl. Phys. Lett. **88**, 143510 (2006)
113. L. Weinhardt, C. Heske, E. Umbach, T.P. Niesen, S. Visbeck, F. Karg, Appl. Phys. Lett. **84**, 3175 (2004)
114. J.F. Moulder, W.F. Stickle, P.E. Sobol, K.D. Bomben, *Handbook of X-ray Photoelectron Spectroscopy* (Physical Electronics, Eden Prairie, 1995)
115. J. Fritsche, S. Gunst, A. Thissen, R. Gegenwart, A. Klein, W. Jaegermann, Mater. Res. Soc. Symp. Proc. **668**, H5.1 (2001)
116. F. Rüggeberg, A. Klein, Appl. Phys. A **82**, 281 (2006)
117. Y. Yoshino, K. Inoue, M. Takeuchi, K. Ohwada, Vacuum **51**, 601 (1998)
118. A. Ohtomo, M. Kawasaki, I. Ohkubo, H. Koinuma, T. Yasuda, Y. Segawa, Appl. Phys. Lett. **75**, 980 (1999)
119. W.R.L. Lambrecht, B. Segall, Phys. Rev. B **41**, 2832 (1990)
120. D. Hariskos, S. Spiering, M. Powalla, Thin Solid Films **480–481**, 99 (2005)
121. T. Negami, T. Aoyagi, T. Satoh, S. Shimakawa, S. Hayashi, Y. Hashimoto, in *Proceedings of the 29th IEEE Photovoltaic Specialists Conference*, New Orleans, USA, 2002, p. 656
122. R. Hunger, T. Schulmeyer, A. Klein, W. Jaegermann, K. Sakurai, A. Yamada, P. Fons, K. Matsubara, S. Niki, Surf. Sci. **557**, 263 (2004)

123. T. Schulmeyer, R. Hunger, W. Jaegermann, A. Klein, R. Kniese, M. Powalla, in *Proceedings of the 3rd World Conference on Photovoltaic Energy Conversion*, Osaka, Japan, 2003, p. 2O.C10.05
124. R. Herberholz, U. Rau, H.W. Schock, T. Haalboom, T. Gödecke, F. Ernst, C. Beilharz, K.W. Benz, D. Cahen, Eur. Phys. J.: Appl. Phys. **6**, 131 (1999)
125. T. Schulmeyer, R. Hunger, M. Lebedev, W. Jaegermann, A. Klein, R. Kniese, M. Powalla, Thin Solid Films **480–481**, 110 (2005)
126. D. Schmid, M. Ruckh, F. Grunwald, H.W. Schock, J. Appl. Phys. **73**, 2902 (1993)
127. D. Schmid, M. Ruckh, H.W. Schock, Appl. Surf. Sci. **103**, 409 (1996)
128. C. Loreck, I. Lauermann, A. Grimm, R. Klenk, M. Bär, S. Lehmann, S. Sokoll, M.C. Lux-Steiner, F. Erfurth, L. Weinhardt, C. Heske, S. Visbeck, T.P. Niesen, C. Jung, C.H. Fischer, in *Proceedings of the 21st European Photovoltaic Solar Energy Conference*, Dresden, Germany, 2006, pp. 1874–1877
129. R.C. Weast (ed.), *CRC Handbook of Chemistry and Physics*, 65th edn. (CRC, Boca Raton, 1985)
130. M. Chase, *NIST-JANAF Thermochemical Tables*, 4th edn. J. Phys. Chem. Ref. Data, Monograph 9 (1998)
131. R. Hunger, P. Fons, K. Iwata, A. Yamada, K. Matsubara, S. Niki, K. Nakahara, H. Takasu, Mater. Res. Soc. Symp. Proc. **668**, H8.21.1 (2002)
132. A. Klein, T. Löher, C. Pettenkofer, W. Jaegermann, J. Appl. Phys. **80**, 5039 (1996)
133. A. Klein, T. Löher, C. Pettenkofer, W. Jaegermann, in *Proceedings of the 14th European Photovoltaic Solar Energy Conference*, Barcelona, Spain, 1997, pp. 2068–2071
134. A. Klein, W. Jaegermann, Appl. Phys. Lett. **74**, 2283 (1999)
135. A. Klein, J. Fritsche, W. Jaegermann, J.H. Schön, C. Kloc, E. Bucher, Appl. Surf. Sci. **166**, 508 (2000)
136. A. Klein, F. Säuberlich, B. Späth, T. Schulmeyer, D. Kraft, J. Mater. Sci. **42**, 1890 (2007)
137. I. Lauermann, C. Loreck, A. Grimm, R. Klenk, H. Mönig, M.C. Lux-Steiner, C.H. Fischer, S. Visbeck, T.P. Niesen, Thin Solid Films **515**, 6015 (2007)
138. B. Chapman, *Glow Discharge Processes* (Wiley, New York, 1980)
139. J. Hedström, H. Ohlsen, M. Bodegård, A. Kylner, L. Stolt, D. Hariskos, M. Ruckh, H.W. Schock, in *Proceedings of the 23rd IEEE Photovoltaic Specialists Conference*, Louisville, USA, 1993, p. 364
140. C. Platzer-Björkman, T. Törndahl, J. Kessler, L. Stolt, in *Proceeding of the 20th European Photovoltaic Solar Energy Conference*, Barcelona, Spain, 2005
141. T. Schulmeyer, A. Klein (unpublished results)
142. Ü. Özgür, Y.I. Alivov, C. Liu, A. Teke, M.A. Reshchikov, S. Dogan, V. Avrutin, S.J. Cho, H. Morkoç, J. Appl. Phys. **98**, 041301 (2005)
143. C. Platzer-Björkman, J. Lu, J. Kessler, L. Stolt, Thin Solid Films **431–432**, 321 (2003)
144. C. Platzer-Björkman, T. Törndahl, D. Abou-Ras, J. Malmström, J. Kessler, L. Stolt, J. Appl. Phys. **100**, 044506 (2006)
145. D. Hariskos, M. Ruckh, U. Rühle, T. Walter, H.W. Schock, J. Hedström, L. Stolt, Sol. Energ. Mater. Sol. Cell. **41–42**, 345 (1996)
146. A. Strohm, L. Eisenmann, R.K. Gebhardt, A. Harding, T. Schlötzer, D. Abou-Ras, H.W. Schock, Thin Solid Films **480–481**, 162 (2005)

147. N. Naghavi, S. Spiering, M. Powalla, B. Cavana, D. Lincot, Prog. Photovolt. Res. Appl. **11**, 437 (2003)
148. S. Spiering, A. Eicke, D. Hariskos, M. Powalla, N. Naghavi, D. Lincot, Thin Solid Films **451**–**452**, 562 (2004)
149. R. Diehl, R. Nitsche, J. Cryst. Growth **28**, 306 (1975)
150. T. Godecke, K. Schubert, Z. Metallkunde **76**, 358 (1985)
151. S. Spiering, D. Hariskos, M. Powalla, N. Naghavi, D. Lincot, Thin Solid Films **431**, 359 (2003)
152. R. Nomura, K. Konishi, H. Matsuda, Thin Solid Films **198**, 339 (1991)
153. A. Timoumi, H. Bouzouita, M. Kanzari, B. Rezig, Thin Solid Films **480**, 124 (2005)
154. Q. Nguyen, U. Rau, M. Mamor, K. Orgassa, H.W. Schock, J.H. Werner, in *Proceedings of the 17th European Photovoltaic Solar Energy Conference*, München, Germany, 2001, p. 1107
155. Q. Nguyen, K. Orgassa, I. Kötschau, U. Rau, H.W. Schock, Thin Solid Films **431**–**432**, 330 (2003)
156. A. Yamada, K. Matsubara, K. Sakurai, S. Ishizuka, H. Tampo, P.J. Fons, K. Iwata, S. Niki, Appl. Phys. Lett. **85**, 5607 (2004)